PNAS

# Supplementary Information for
Rubble pile asteroids are forever

**Authors:** Fred Jourdan[1,2,3], Nicholas E. Timms[3], Tomoki Nakamura[4], William D.A. Rickard[2], Celia Mayers[2], Steven M. Reddy[3], David Saxey[2], Luke Daly[5,6,7], Phil A. Bland[3], Ela Eroglu[8], Denis Fougerouse[2,3]

**This PDF file includes:**

Supplementary Text
Figs. S1 to S57
Table S1 to S5
SI References

**Other Supplementary Materials for this manuscript include the following:**

Dataset S1: EMPA analyses of three Itokawa particles
Dataset S2: APT analyses of one Itokawa particles
Dataset S3: $^{40}Ar/^{39}Ar$ analyses of three Itokawa analyses

# Supplementary information text

1. Mineralogy and mineral compositions of the particles via SEM imaging and EDX and EMPA data.

All EMPA data are provided in Dataset S1 and are used to verify the nature of each type of mineral obtained by other techniques, as well as securing compositional information before melting each particle for $^{40}Ar/^{39}Ar$ dating. Note that on occasion totals do not reach 100% and data points with total < 98 % should be treated with caution. For the purpose of this study, however, the level of quality of all these data is enough and corroborate well the petrographic information obtained by other techniques.

*1.1. Particle RA-QD02-0059*

This particle is ca. 191 µm in its longer side with an elongated shape and consists of olivine, plagioclase and troilite (Fig. S4). Its aspect is typical of a metamorphosed and equilibrated rock. Fig. S5 and Table S1 gives the concentration of elements in the various phase constituent of particle #0059. Fig. S6 show the location of EMPA spot analysis. Plagioclase is albitic (Na:Ca = 6.2; $Or_{3.3}$-$An_{8.2}$-$Ab_{88.5}$; Dataset S1)) and EMPA data (Fig. S7) shows that it contains only 0.6 wt% of K. It is therefore slightly depleted K compared to the plagioclase from other particles which shows K composition of ~ 0.8-1% wt. % (1 and this study). Fig. S8 shows the specific area consisting of plagioclase and targeted for Time-of-flight secondary ion mass spectrometry (ToF-SIMS) chemical mapping.

*1.2 Particle* RA-QD02-0288

This particle is ca. 169 x 142 µm in size (Fig. S9) and Fe-SEM and EDS observations suggest that this particle consists of Ca-rich and Ca-poor pyroxene and olivine (Fig. S9). Although plagioclase was initially described by JAXA, no plagioclase was observed at the Tohoku University during BSE imaging and therefore, no plagioclase could be analysed using the EMPA instrument. After subsequent repolishing at Curtin University, minor amount of plagioclase was observed (Fig. S9). Although the amount of plagioclase in this 2D observation looks minor (Fig. S9-10), the abundant amount of $^{40}Ar^*$ gas during $^{40}Ar/^{39}Ar$ step-heating extraction attests that this particle is plagioclase bearing. Plagioclase contains ~ 0.8 wt.% K and is albitic in composition (Na:Ca = 5; Table S2). Fig. S11 shows the map distribution of EMPA analyses and Fig. S12 shows the CaO and Al2O3 composition of low-Ca pyroxene demonstrating that pyroxene is relatively homogenous. All analyses are provided in Dataset S1 and show that other crystals are equally homogenous. Fig. S13 shows the two areas targeted for ToF-SIMS analysis which consist of a plagioclase-pyroxene boundary and an olivine – low-Ca pyroxene – high-Ca pyroxene triple junction.

*1.3 Particle* RA-QD02-0010

This particle is ca. 149 µm in its longer side (Fig. S14) and is rounded. It consists of olivine, plagioclase (Fig. S15), low- and high-Ca pyroxene, troilite, taenite and kamacite (Fig. S14). The crystal texture of this particle is typical of a metamorphosed and equilibrated rock with a pyroxene equilibration temperature calculated at 837 ± 10 °C (a full description published by Nakamura, *et al.* (2)). EMPA data (Fig. S16) shows that plagioclase contains an average of ~ 0.9 wt% of $K_2O$ and is homogenous in composition (Fig. S17). Plagioclase is albitic (Na:Ca = 4.2; $Or_{5.4}$-$An_{11.4}$-$Ab_{83.2}$; Dataset S1) as shown in Table S3. Fig. S18 shows the two areas targeted for ToF-SIMS analysis and which consists of plagioclase twin boundaries and a plagioclase-troilite phase boundary (area 1), and a small plagioclase crystal within a large olivine crystal (area 2).

2. Electron Backscatter Diffraction (EBSD)

A $^{40}Ar/^{39}Ar$ age provides information on when a given mineral was raised above and subsequently cool down below its $^{40}Ar^*$ closure temperature and, either indicates the age of crystallization / metamorphic cooling of the particle, or the age of an impact event. However, such an age information is significantly less useful if the shock state of the particle is not known, hence the need for careful petrographic observations, and EBSD analyses (Fig. 1) which both provide information on the P-T conditions during an impact event.

*2.1 Particle RA-QD02-0288*

The grains in particle RA-QD02-0288 have gently curved grain boundaries and ~120º triple junctions (Fig. S19). All phases yield strong, indexable EBSD patterns, and are therefore highly crystalline (Fig. S19). All phases preserve very low degrees of intragrain misorientation (Fig. S20). High-Ca pyroxene preserves minor irregular low-angle (<1º) boundaries towards the margins of the particle (Fig. S20). All observations are consistent with the microstructure resulting from high-temperature equilibration, during which mobility of dislocation and grain boundaries acted to reduce the internal strain energy and interface energy of the microstructure, respectively. The thermally-equilibrated microstructure is cross cut by irregular brittle fractures that are not accompanied by any evidence of shock deformation (Fig. S20).

*2.2 Particle RB-QD04-0059*

The grains in particle RA-QD04-0059 typically have gently curved grain boundaries and ~120º triple junctions (Fig. S21). All phases yield strong, indexable EBSD patterns, and are therefore highly crystalline (Fig. S21). Note that plagioclase yielded weaker EBSD patterns in the 80 nm step size map of the entire particle due to slightly different electron beam conditions, yet were strong and indexable in the 100 nm step size map of the central area of the particle. All phases preserve very low degrees of intragrain misorientation (Fig. S22). The olivine, troilite, and taenite preserve minor irregular low-angle (<1º) boundaries towards the margins of the grains (Fig. S22). All observations are consistent with the microstructure resulting from high-temperature equilibration, during which mobility of dislocation and grain boundaries acted to reduce the internal strain energy and interface energy of the microstructure, respectively. The

thermally-equilibrated microstructure is cross cut by irregular brittle fractures that are not accompanied by any evidence of shock deformation (Fig. S22).

*2.3 Particle RA-QD02-0010*

The grains in particle RA-QD02-0010 typically have gently curved grain boundaries and ~120º triple junctions (Fig. S23). All phases yield strong, indexable EBSD patterns, and are therefore highly crystalline (Fig. S23). All phases preserve very low degrees of intragrain misorientation (Fig. S24). Some olivine grains preserve a few irregular to planar low-angle (<1º) boundaries, with the highest cumulative misorientation at triple junctions and at the margin of the particle (Fig. S24). All observations are consistent with the microstructure resulting from high-temperature equilibration, during which mobility of dislocation and grain boundaries acted to reduce the internal strain energy and interface energy of the microstructure, respectively. The thermally-equilibrated microstructure is cross cut by irregular brittle fractures that are not accompanied by any evidence of shock deformation (Fig. S18). Some misorientation can be seen across some fractures, which is consistent with minor amounts of rigid block rotation associated with brittle fracturing (Fig. S24).

3. ToF-SIMS

The distribution of K (± Ca and ± Na) is important when conducting $^{40}Ar/^{39}Ar$ dating analysis, particularly when several mineral phases are present, and the sample had a complex time-temperature history. Each mineral is likely to have a different closure temperature to Ar diffusion and therefore, will record different age-related information. ToF-SIMS allows high-spatial resolution mapping of elements and isotopes at the single crystal level and thus can assess compositional homogeneity (3).

*3.1 Particle RA-QD02-0288*

ToF-SIMS analysis shows that the plagioclase composition of this particle (picture in Fig. S25) is generally homogeneous albeit depletion of $^{39}K$ and $^{23}Na$ along cracks (Fig. S26). No K-feldspar exsolutions are present in the plagioclase. Similarly pyroxene shows enrichment of Mg, Si, Ca and Fe along cracks and grain boundaries (Fig. S26), possibly associated with Fe-rich fluid metasomatism on the monolithic parent body such as proposed for asteroid Vesta (4), albeit this is beyond the scope of this study.

We also analysed olivine and, low-Ca and high-Ca pyroxene to test if any $^{39}K$ could be detected by ToF-SIMS, and if yes, if it could be a contributor of the total $^{40}Ar^*$ budget within Itokawa's particle (Fig. S27). This is important since it has been shown that pure pyroxene contains slight amount of $K_20$ and can be dated by the $^{40}Ar/^{39}Ar$ technique (5, 6) and since plagioclase and pyroxene have different responses to Ar diffusion and therefore could affect the shape of $^{40}Ar/^{39}Ar$ age spectra. Interestingly, Fig. S27 seems to suggest the presence of measurable $^{39}K$ in high-Ca pyroxene, however, inspection of the raw data fails to show a K peak, and the signal in fact arises from the tail of Ca captured during the scan around mass 39.

As such, if K is present in any of those phases, its concentration is well below the detection limit and thus suggest no influence on the $^{40}Ar^*$ budget.

*3.2 Particle RA-QD04-0059*

ToF-SIMS analysis of particle #0059 shows that plagioclase is fairly homogenous and does not contain large or feather-like K-feldspar exsolutions, contrary to particles #0013 (1) and #0010 (this study), respectively (Fig. S28-29). Grain scale elemental mapping by SEM EDS revealed that the plagioclase phase was the only phase that hosted K above the detection limit. Higher spatial resolution and sensitivity analysis by ToF-SIMS focused on the plagioclase region to investigate the K distribution in greater detail. This analysis did not find any significant heterogeneity of K distribution supporting the premise that the $^{40}Ar^*$ signal arises from a chemically uniform plagioclase crystal.

*3.3 Particle RA-QD02-0010*

Some preliminary ToF-SIMS data from this particle have been presented by (3) to illustrate the work flow between ToF-SIMS and atom probe tomography analyses, but not geological discussion was given. Hereafter, we present a selection of results from selected regions of interest (ROIs; Fig. S30) analysed with ToF-SIMS, that are most relevant to this work. Of particular interest for the present study is the abundance of K-rich domains in plagioclase. ToF-SIMS is particularly sensitive to alkali metals and therefore, map such as $^{39}K$ had a particularly high signal to noise ratio, which facilitated the observation of the K-rich features. Those features are often located at the twin boundaries (Fig. S31-34) and are fairly small in size. However, the spatial resolution of the ToF-SIMS analyses is insufficient to resolve the size of these exsolutions, which is important for two reasons. Firstly, a good approximation of the dimensions of the exsolutions is useful for the diffusion model applied to particle #0010 and presented later in the text. Secondly, considering that exsolutions that small have never been observed before to the best of our knowledge, it was important to obtain as much information as possible before melting the particle for $^{40}Ar/^{39}Ar$ analysis. The atom probe tomography results indicate that the K-rich features are exsolution of K-feldspar (Fig. S32; Dataset S2) and while they are up to a micron long, they are only ~ 10-15 nm wide. The combined volume of the K-feldspar exsolutions within plagioclase is hard to determine, but due to their high-K content, even 5 % vol. K-feldspar would still represent 40% of the $^{40}Ar^*$ total budget (cf. diffusion model in a later section). A small plagioclase crystal within olivine (ROI 7; Fig. S33) shows similar level of exsolutions albeit some of them seem to be occurring in the middle of the plagioclase crystals rather than at its boundaries or twin boundaries. Worth noting is an enrichment in Ca and Na in plagioclase on the left-hand side region of Fig. S33, which cause could be related to an edge effect and detector saturation. ToF-SIMS analysis of the side of a TEM foil extracted from the cross-section of the ROI revealed that the K-feldspar exsolutions are occurring in depth within the crystal and radiating in 3 dimensions from the twin boundaries. Note that the feather-like K-feldspar exsolutions are very different from the single 15 x 1 µm K-feldspar exsolution lamellae found in particle RA-QD02-0013 (Fig. S35) and reported by (1). The reason for the difference is unclear but might be due to the speed of cooling

following peak metamorphism in the monolithic parent body or due to impact-related reheating.

## 4. $^{40}Ar/^{39}Ar$ data

### *4.1 Particle RA-QD02-0288*

Particle #0288 yielded a $^{40}Ar$ beam signal of 92 fA (Dataset S2), similar to particle #0013 (93 fA) from which we obtained an age of 2291 ± 139 Ma (1), and a $^{39}Ar$ signal with a value of 0.21 fA. We calculated a plateau age of 4219 ± 35 Ma (2σ; MSWD = 0.8; P=0.58; Fig. 2 and S36) which include 81% of the total $^{39}Ar$ released. The slight spread of data along the isochron is largely based on a single point and allowed us to calculate an inverse isochron age of 4213 ± 57 Ma (P = 0.06; Fig. S37) with an $^{40}Ar/^{36}Ar$ intercept value of 1.3 ± 0.5 (Fig. S37), largely indistinguishable from the plateau age calculated using a value of 1 ± 1. Due to the low spread and poor level of concordance of the inverse isochron data, we have adopted the plateau age in this study. Note that highest heating step (< 3 % of the total $^{39}Ar$) show a slightly younger apparent age. This process is often observed for multi-mineral samples where different $^{40}Ar^*$ reservoirs will diffuse $^{40}Ar^*$ differently when exposed to ultra-transient shock events caused by very small impacts. In particularly plagioclase and pyroxene (± olivine) have been shown through diffusion experiments and modelling and direct observations to undergo a kinetic crossover in their diffusion characteristics for ultra-transient and ultra-high temperature impacts (7-11). Such conditions are generally caused by small localized impacts and only affect pyroxene. Despite a temperature of few thousands of degrees, the extremely short durations of micro- to milliseconds associated with these events leave the Ar* budget in the plagioclase untouched while causing $^{40}Ar^*$ diffusion in pyroxene (7-9, 11). This interpretation is corroborated by the decrease of K/Ca at high temperature associated with pyroxene (Fig. S37).

### *4.2 Particle RA-QD04-0059*

Particle #0059 yielded a $^{40}Ar$ beam signal of 60 fA and a $^{39}Ar$ signal with a value of 0.15 fA (Dataset S2). We calculated a plateau age of 4149 ± 41 Ma (2σ; MSWD = 1.3; P=0.27; Fig. 2 and S39) which includes 89% of the total $^{39}Ar$ released. The data defined no spread along the inverse isochron and the plateau age was calculated using a value of 1 ± 1 (Fig. S40). The K/Ca plot (Fig. S41) shows K/Ca values indistinguishable from the background level, probably due to the lack of Ca. As observed for particle #0288, the high-temperature extraction steps (< 10 % $^{39}Ar$) of the age spectrum show younger apparent ages. Whereas no pyroxene is observed, the modal volume of particle #0059 is dominated by olivine which has also be shown to be able to contain trace of K and thus be able to produce small amount of $^{40}Ar^*$ (12). The diffusion characteristics of Ar in olivine are still poorly known except for the isolated study by (12) and our preferred interpretation is that the last part of the spectrum is dominated by olivine which, like pyroxene, has been affected by a small impact with an overall energy level insufficient to affect plagioclase.

### *4.3 Particle RA-QD02-0010*

Particle #0010 yielded a $^{40}Ar$ beam signal of 61 fA and a $^{39}Ar$ signal with a value of 0.03 fA (Dataset S2). The age spectrum is defined by a hump-shaped pattern and no age could be calculated (Fig. 2 and S42). The youngest apparent step-age obtained at low temperature extraction is around 500 Ma suggesting a thermal perturbation at, or younger than 500 Ma. The data defined are scattered also on the inverse isochron plot (Fig. S43), preventing to derive an age. The K/Ca plot show K/Ca values indistinguishable from the background level, probably due to the lack of Ca (Fig. S44). The cause of the shape of the age spectrum of particle #0010 will be discussed hereafter.

## 5. Cooling and diffusion models

### 5.1 Slow cooling inside the monolithic parent

Petrographic observations indicate that these particles experience equilibration and thermal metamorphism in the monolithic parent body to temperature up to 800 °C implying a depth of few tens of kilometres (2, 13). The episode of peak metamorphism was followed by a period of slow cooling inside the asteroid hence raising the possibility that the two ~ 4.2 Ga ages obtained in this study recorded a simple monotonic cooling history in the parent body, particularly since no to little shock is observed for each of the particles. Here, we use the thermal model scenario of (14) and use a thermal solution for a particle located at a depth of 30 km and that reached a peak metamorphism of ~ 900 C (100 °C more than measured by petrography to be on the safe side). The model predicts that the particle will cool down to 250 °C, in about ~ 150 million years. We then model the effect of such a slow cooling scenario on an albitic plagioclase using the ArArDIFF algorithm (1, 15) which allows interrogating the effect of thermal diffusion from a particular time-temperature history on a given $^{40}Ar/^{39}Ar$ age spectrum. In detail, we modelled an initial increase of temperature from 0 to 800 °C, from 4565 to 4560 Ma, followed by a monotonic cooling from 800 to 250 °C from 4560 to 4410 Ma and then from 250 to 0 °C until 4000 Ma. We used average $D_0$ and $E_a$ values of 5 x $10^3$ $cm^2/s$ and 290 kJ/mol *(16)* and the crystal dimensions were approximated by a sphere of 20 µm. Fig S45 compares then the synthetic age spectrum from our model (blue boxes) with the actual results from particle #0288 (pink dashed boxes). Our diffusion model show that the slow cooling scenario fail to reproduce our results well beyond uncertainty and would rather generate an apparent plateau age of 4439 (± 35) Ma instead of 4219 ± 35 Ma, hence more than 200 Ma older. Based on those results, we conclude that the slow cooling scenario is very unlikely to have generated the 4.2 Ga $^{40}Ar/^{39}Ar$ ages.

### *5.2 Time-temperature-Porosity Monte Carlo simulation modelling*

In order to explain was the K/Ar systematics of particle #288 and #0059, we have modelled the effect of $^{40}Ar^*$ loss on a small plagioclase crystal (the main carrier of $K_2O$ for these two Itokawa particles) for a range of pressure-porosity-temperature solutions initially presented by (1) and using a Monte Carlo simulation approach (15) applied to a diffusion equation for spherical geometry (17). Such an approach takes into account the large number of adjustable

parameters and/or uncertainties. We calculated the resulting post-shock temperature based on randomized discreet levels of pressure (5, 10, 15, 20 and 25 GPa) and porosity values ranging from 1% to 50% from the pressure-porosity-temperature model from (1). We used a set of defined pressure values instead of a continuous pressure range from 5 to 25 GPa in order to be able to better identify the effect to each pressure values on the level of $^{40}Ar^*$ loss. The cooling time following each calculated post shock temperature was calculated assuming an idealized perfect black body following details given by (18) and (1) and using the following final equation reported by these authors:

$$t = \frac{r\,\rho\,C_p}{9\sigma}\left[\frac{1}{T^3} - \frac{1}{T_i{}^3}\right] \qquad (1)$$

where r is radius of a sphere (m), ρ is density (kg/m$^3$), Cp is the heat capacity at constant pressure (j kg$^{-1}$ K$^{-1}$), σ is the Stefan-Boltzmann constant (5.670373 × 10$^{-8}$ kg s$^{-3}$ K$^{-4}$), and $T_i$ is the initial (maximum temperature) in Kelvin. The variables for the present system were taken as a sphere; ρ for basalt was assumed to be around 3000 kg/m$^3$ (19), and Cp of basalt was approximately 840 j kg$^{-1}$ K$^{-1}$ (20). The particle at the beginning of the process ($t_0$ = 0 s) has an initial maximum temperature of $T_i$ calculated as per described above. The lower limit of our cooling model is set at 200°C where $^{40}Ar$ has already completely stopped diffusing out of the system at those relatively short timescales. We assume that each particles was located in central position within boulders with radius ranging from 0.1 m to 25 m (2). The resulting cooling durations ranged from ca. 177 seconds to 13.4 days.

Note that the temperature calculated above represent the total cooling time from the maximum post-shock temperature to 200°C. However, the cooling of natural system is not linear and our cooling calculation follows a logarithmic curve to mimic natural system that spent shorter amount of the time in the high temperature regime and significantly longer time in the low temperature regime (Fig S46).

We used the following diffusion parameters: Albite ($D_0$ = 5 x 10$^3$ cm²/s; $E_a$ = 290 kJ/mol) with a radius of 20 µm with diffusion values taken from Cassata and Renne (16). we also model orthopyroxene ($D_0$ = 6 x 10$^2$ cm²/s; $E_a$ = 371 kJ/mol; Cassata, Renne and Shuster (7)) with a radius of 30 µm albeit EDX and ToF-SIMS Dataset Suggest that this phase contribution to the $^{40}Ar^*$ budget is negligible. The range of values and/or associated uncertainties modelled for each parameter given in Table S4.

We simulated 10,000 trials using the statistical software package Quantum XL©, a commercially available Excel add-on from Sigmazone©. Results are presented in Fig. 3 in the main text, and Fig. S47 and S48. Fig. S47 and S48 are complimentary to Fig. 3 and show the proportion of $^{40}Ar^*$ loss in function of pressure and porosity (and indirectly calculated maximum post-shock temperature). Full reset of the K/Ar system is considered when the simulations return $^{40}Ar^*$ loss values ≥ 0.99. This necessitates inversely correlated pressure-porosity values between ca. 8 GPa with 50% porosity to 25 GPa with 21% porosity.

Tornado charts (i.e., percent contribution analysis (15); Fig. S49) show that the variation in the fraction of $^{40}$Ar* loss is controlled at 73% by the amount of porosity and 27% by the shock pressure during the impact, with the ranges of all other parameters playing a negligible role in the variation of $^{40}$Ar* loss. In details however, the $^{40}$Ar* loss variation is in fact controlled by the maximum value of the post-shock temperature, and this is the latter factor which is controlled by the amount of porosity and shock pressure level (Fig. S49; Fig. 3).

Fig. S50 shows that a minimum temperature of ~ 920 °C is required to fully reset plagioclase within the cooling time frame of a few days, as allowed by our calculations. If orthopyroxene is taken into account, its much higher activation energy requires the system to reach a minimum temperature of ~1400 °C (Fig. S50). This correspond to a minimum possible pressure of ca. 12 GPa for porosity of 50%. For pressure levels of 25 GPa, this necessitates a minimum porosity of 30 %. However, note that pyroxene is a phase with very low level of K and thus, will have very low level of $^{40}$Ar* accumulated (5, 6). That implies that the contribution of pyroxene will be barely noticeable (few % of the total $^{39}$Ar released) to the $^{40}$Ar* budget of the tiny Itokawa particles, and as such, a plagioclase-pyroxene particle (groundmass; blue circles in Fig. S50), will essentially behave like pure plagioclase. As discussed above, the small possible contribution from pyroxene might be further affected by ultra-transient heating events as well.

Finally, Fig. S51 shows that the lack of correlation between $^{40}$Ar* loss and cooling time suggests that the cooling duration plays only a minor role in the process associated with $^{40}$Ar* loss, and conversely, as illustrated by the tornado chart, porosity and pressure are the two dominant factors.

*5.3 Hot blanket Monte Carlo simulation modelling*

We have simulated the effect of the time-temperature history on the $^{40}$Ar* budget of an unshocked particle which has been embedded in a hot insulating blanket. In this scenario, an initially unshocked cold rock or boulder has been excavated during a catastrophic breakup from few kilometres deep within the asteroid where it was initially equilibrated. This rock has then been re-amalgamated into a large rubble pile asteroid where the cold fragments were then put in contact with strongly shocked and heated fragments. Heated fragments were initially located within or nearby the large impact which caused the breakup of the monolithic parent body. The result is that the cold rock, particularly if relocated deep within the newly-formed rubble pile, was heated to few hundred degree and slowly cooled down. A slow cool down is rendered possible thanks to the insulating layer formed by superimposed rubble pile material as shown in the reassembly scenario proposed by (21) who estimated cooling rate of 1 to 10 °C/Ma for reassembled fragments of an initially hot parent chondritic parent body. Following this scenario, such a rock is gradually excavated to the surface during the ≥ 4.2 Ga life of the rubble pile asteroid due to collisions and material loss directly into space (22). We used a similar approach and parameters (Table S4) as described for the temperature-pressure-porosity model described above, except that the maximum post-shock temperature and total cooling duration values were not calculated but were considered as direct inputs. Temperature and cooling randomized values range from 800 to 300 °C and 13 days to 1 Ma, respectively and cooling

follow a logarithmic decay function as described for the temperature-pressure-porosity model (Fig. S46).

Fig. S52 shows that for total cooling durations between 1000 years to 100,000 years, the peak temperature must reach at least inversely correlated values ranging from ~700°C to 517°C. Durations from 100,000 years to 1 million years required inversely correlated peak temperatures ranging from 517°C to 465 °C showing that beyond a duration of 100,000 the total duration play a lesser role in diffusing $^{40}$Ar*, compared to the maximum value of the post-shock temperature (Fig. S53).

6. Thermal history of particle RA-QD02-0010.

Particle #0010 yielded a perturbed hump-shaped age spectrum with apparent step-ages increasing from ~0.5 Ga to ~4.2 Ga and decreasing again to ~ 1.8 Ga at high extraction temperature. EBSD analysis of particle #0010 reveals that, of the three particles analysed in this study, this is the particle that presents the most evidence of shock process (Fig. 1 and S24). Yet, even for this particle, the estimated level of shock is relatively low with estimated pressure values around 10 – 15 GPa, although precise values are hard to estimate. No other shock diagnostic features are present suggesting that the shock level stayed well below 25 GPa (23, 24). ToF-SIMS and atom probe tomography analyses of the K composition of plagioclase crystal show dendritic (feather-like) K-feldspar exsolutions that are few micrometres long and tens of nanometres wide and which occurred exclusively at twin and phase boundaries (Fig. S29-34; 3).

Whereas hump shaped $^{40}$Ar/$^{39}$Ar age spectra with dramatic step age variations have been attributed to the effect of ultra-transient heating events on several phases exhibiting a kinetic crossover of diffusion parameters at very high temperature (7, 10; cf. discussion above), this effect has been largely confined to plagioclase-pyroxene bearing meteorites. Here, we tested if the effect of kinetic crossover could be observed between plagioclase and the micron-size K-feldspar exsolutions present at the grain boundary of plagioclase (Fig. S29-34). We model the effect of an ultra-transient heating event on a binary mixture of sanidine and albitic plagioclase using the ArArDIFF algorithm (1, 15) which allows interrogating the effect of thermal diffusion from a particular time-temperature history on a given $^{40}$Ar/$^{39}$Ar age spectrum. We used average $D_0$ and $E_a$ values of 6.7 x $10^{-1}$ cm$^2$/s and 220 kJ/mol and 5 x $10^3$ cm$^2$/s and 290 kJ/mol (16) and the crystal dimensions were approximated by spheres with radii of 3 µm and 25 µm for sanidine and albite, respectively. We used a modal composition of 5% sanidine and 95% albite (Fig. S29-34), but to their different in $K_2O$ content (10% and 1% for sanidine and albite, respectively) the relative contribution of each phase in the mixture is 40% and 60% respectively. It is important to note that we are not trying to invert the precise T-t history of the crystals, but to test if the diffusion kinetic cross-over between sanidine exsolutions and albite during a high-temperature ultra-transient event could explain the shape of the age spectrum obtained for particle #0010. Due to their diffusion characteristics, both phases degas at different temperature in the laboratory, with the initial degassing of the sanidine at low to

mid-temperatures (red curve, Fig. S54) and albite at mid- to high-temperatures (green curve, Fig. S54) hence have some level of decoupling.

We tested the effect of an impact at 200 Ma on a 4560 Ma particle with the heat wave having a duration of 0.4 µs and temperature values of 3000, 4500 and 8000 °C (Fig. S55) and compare the synthetic age spectra (solid blue boxes) with the results obtained for particle #0010 (orange dash-line boxes). Whereas a temperature around 3000 °C is not sufficient to trigger a kinetic crossover and shows only $^{40}$Ar* loss at low temperature extraction steps (from the sanidine phase; Fig. S55a), temperatures of 4500°C and 8000 °C both caused a clear humped-shape $^{40}$Ar/$^{39}$Ar age spectrum (Fig. S55b,c), of which, a temperature of 4500 °C best reproduces the age spectrum from particle #0010 (Fig. S55b). All diffusion and thermal parameters are given in Table S5.

These results therefore suggest that particle #0010 was affected by an ultra-transient impact event around 0.5 Ga or younger. As mentioned for particles #0288 and #0059, such a high temperature is incompatible with the increase of temperature expected for low shock level of 10 - 15 GPa. In the present case, the level of heat needed to trigger a kinetic crossover is much higher and yet, its duration is much shorter than for particles #0288 and #0059. It is probably explained by the presence of pores and their effect at the mineral scales. Numerical simulations have shown that pore collapse during impact can locally increase the temperature at very specific locations within a rock (25) without the need for high pressure levels and therefore, this is our favourite explanation to explain these particular conditions. This also indicates that either the porosity on Itokawa is slightly heterogeneously distributed, or that various small impacts with a range of energy have occurred Itokawa during its history, or more likely, and quite intuitively, a combination of both effects.

Interestingly, we previously investigated particle #0013 (1) which also contains exsolved sanidine (K-feldspar) within albite, but in the latter case, both phases were equally reset at ~ 2.3 Ga thus necessitating a time-temperature history sustained for much longer than a few microseconds (1), and which duration is similar to one calculated for particles #0288 and #0059 in the present study. The difference between the two scenarios (full reset vs. partial reset + kinetic crossover) might be associated with full compaction of the rock upon impact in the first case, vs very localized pore collapses in the second case. An age ≥ 4.2 Ga for the monolith parent disruption implies that partial reset (#0010) or full reset (#0013; ~ 2.3 Ga; (1)) of the K/Ar system after that time were triggered within the context of porous medium rather than by hot blanketing.

## 7. Discussion of the available isotopic ages

### *7.1 Robust ages*

All radioisotopic age results are shown in Fig. S56. A single-particle $^{40}$Ar/$^{39}$Ar plateau age of **2.29 ± 0.14 Ga** was obtained on particle RA-QD02-0013 by (1) which they interpret as a minimum age for the formation of Itokawa. Two single-particle $^{40}$Ar/$^{39}$Ar plateau ages of **4.22**

**± 0.04 Ga** and **4.15 ± 0.04 Ga** were obtained on particles RA-QD02-0288 and RA-QD04-0059, during the course of this study. A U-Pb phosphate age of **4.64 ± 0.36 Ga** (uncertainties given at 2σ for comparison) was obtained by (26) on particle RA-QD02-0056 and interpreted by these authors as indicating the age of the thermal metamorphism occurring on the initial monolithic parent body. All these ages are considered robust and statistically valid in this study.

*7.2 Flawed / ambiguous ages*

An $^{40}Ar/^{39}Ar$ age of 1.3 ± 0.3 Ma was initially obtained by (27) but was obtained by pooling three dust particles (RA-QD02-0199, RB-CV-0002 and RB-CV-0051) from two different landing sites together. No petrographic characterizations of the shock level of each particle was attempted. However, since it is more than likely that each particle has their own time temperature history, the meaning of an apparent age of ~1.3 Ga from a mixture of uncharacterized material is hard to interpret. A mixture of material with similar diffusion characteristics can lead to meaningless plateau ages simply because the same material (e.g. plagioclase) will have the same lab degassing characteristics for each sample and thus all the gas released from each particle will overlap and result in a meaningless intermediate value (28). For example, we used ArArDIFF to model a mixture of three particles of albite ($E_a$ and $D_0$ values as in Table S5) with sizes of 90, 60 and 50 µm and relative modal compositions of 40, 30 and 20%, respectively, to roughly approximate the particles analysed by (27). These three particles were attributed arbitrary ages of 600, 2800 and 500 Ma, respectively. The mixture was calculated based on the degassing curves and calculated using ArArDIFF algorithm following the mixing approach of VanLaningham and Mark (28) and Jourdan, *et al.* (29). Step uncertainties were input at ± 25% to roughly match the ones obtained by (27). Fig. S57a shows that the laboratory degassing curves largely overlap for the three albite particles and resulted in a well-defined plateau age of ~1.3 Ga (Fig. S57b). However, in our mixture, none of the individual ages were near 1.3 Ga. Of course, this is simply one of the possible mixing scenarios as it is not possible to disentangle the age of each particle using this approach. Nevertheless, our simple model has the merit to illustrate that in this case, an age of 1.3 Ga would bear no geological meaning. In the second example, 85% of the $^{40}Ar^*$ contribution is from the largest particle and the other particles contribute to 15% and 5% of the $^{40}Ar^*$, respectively. In order to match an age of 1.3 Ga, the particles were given ages of 900, 4200 and 500 Ma (Fig. 56c). Note that the very large $^{40}Ar^*$ contribution from the first particle make the age of 900 Ma of this particle relatively close to the final age of 1.3 ± 0.3 Ga, yet, still outside the error envelop.
The possibility of these scenarios were acknowledged by (27) but these authors rather proposed that all particles had the same age, which is extremely unlikely considering the range of single-particle $^{40}Ar/^{39}Ar$ ages obtained so far (this study; 1). Rather, considering its mixture nature, we recommend using the 1.3 Ga age with caution, if at all.

A single-particle $^{40}Ar/^{39}Ar$ plateau age of 5.4 ±1.6 Ga was obtained by (1) on particle RA-QD02-0030. Albeit avoiding the multi-component mixture issue described above, the downside of their analysis was the extremely low $^{39}Ar$ signal recovered from this particle and, thus, its blank-sensitive nature. It yielded an apparent age which bear little significance due to

its very large uncertainty and these authors interpreted this "age" as simply indicating that the particle was likely older than particle #0013.
A phosphate U-Pb Isochron age of 1.5 ± 1.7 Ga was calculated by (26), however, it is important to highlight that this apparent age was derived by mixing data from 4 particles and essentially represent a 2-point isochron, with the majority of the points (cluster 1) being inversely discordant compared to the concordia curve, and the second point given by a single datum largely overlapping the upper age and concordia curve (even within the 1σ envelop given by these authors). Therefore, no isochron line should be drawn to the lower intercept of the concordia in these conditions and this apparent and imprecise age should be considered as a numerical artefact.
The last apparent age is indirectly provided by particle RA-QD02-0010 in this study. According to the time-temperature model shown in Fig. S55, an impact no older than ≤ 0.5 Ga is necessary to explain its hump shape. Although we think our explanation is rather sound, it is rather an indirect mean to derive an age and we recommend using the ≤0.5 Ga age with caution, if at all.

8. Discussion of the effect of solar radiation on $^{40}$Ar* loss

Note that this point has been discussed extensively by (27) and in our previous contribution (1) but is reiterated for the sake of completeness. Jourdan, et al. (1) calculated that the equilibrium temperature at the surface of Itokawa were on the order of 5 °C at perihelion, in agreement with measured surface temperatures ranging from -15 °C to a peak temperature of 30 °C (30, 31). For such low temperature, we showed that none of the feldspar phases would lose any $^{40}$Ar* for the current orbit (1) which was similar to conclusions reached by (27) using a different approach. Various authors have suggested that Itokawa might have a different orbit in a more distant past, possibly as close as the current orbit of Mercury. Considering that asteroid Itokawa is slowly losing material to space (22), that means that the particles present at the current surface were once buried below a layer of regolith. Such particles would not be subjected to peak temperature above 65 °C and numerical modeling using the ArArDIFF algorithm (1) demonstrated that as those temperature, plagioclase is immune to $^{40}$Ar* diffusion loss. As the present study now shows, the presence of two $^{40}$Ar/$^{39}$Ar ages around 4.2 Ga further demonstrates that the K/Ar system in Itokawa's particles has not been noticeably affected by solar heating since that time, and there is very little reason to suspect it was roaming closer to the sun prior to 4.2 Ga.

9. Discussion about the LL-chondrite $^{40}$Ar/$^{39}$Ar database.

Recently, (26) compared their results with the $^{40}$Ar/$^{39}$Ar data available for LL-chondrites. These authors claimed that the $^{40}$Ar/$^{39}$Ar database for LL-chondrite suggest an existing age concentration around 4.2 Ga which was not identified in their U-Pb data. While our $^{40}$Ar/$^{39}$Ar Dataset Show indeed two plateau ages at ~ 4.2 Ga, none of the age spectra published on LL-chondrite define true ages, but instead they represent severely perturbed age spectra (32, 33). Perturbed age spectra such as those are formed as a result of $^{40}$Ar* loss and as such, none of the apparent step-age represent the initial formation age, nor the age of the impact as all step-ages have intermediate values between those two events. Different mineral phases are variably

affected by $^{40}$Ar* loss during an impact heating event (e.g., Fig. S43) and the same mineral phases will degas at different time during laboratory extraction, hence a wavy/structured age spectrum (e.g., Fig. S55). Therefore, those intermediate step-ages or the entire age spectrum cannot be utilised to derive impact ages and can only be used at most to estimate minimum, partially reset ages based on the oldest part of the age spectra (6, 10, 34-37). As such, most $^{40}$Ar/$^{39}$Ar data obtained on LL-chondrite cannot (and should not) be used to define any putative age concentration and clearly, additional geochronological work is needed on LL-chondrites. Rather, as we described in Jourdan, *et al.* (1), only the meteorite Parnallee currently defines a proper $^{40}$Ar/$^{39}$Ar plateau age of 1.9 ± 0.1 Ga for (38, 39), and perhaps the fossil meteorite associated with the Morokweng impact structure where an isochron age of 625 ± 163 Ma was obtained by (40). All other meteorites yielded partially reset $^{40}$Ar/$^{39}$Ar ages only. Furthermore, whereas Itokawa has lost mass to space during its life span, the initial dimensions of the rubble pile are unlikely to exceed a kilometre. This is in contrast with the minimum radius of 20 km predicted for the monolithic parent body based on the equilibration observed in Itokawa's particles (2). Hence this means that the majority of the mass from the shattered monolithic parent body was therefore not included in Itokawa and rather lost or recombined in other rubble piles bodies with a LL-chondrite composition. Further work should include a multi-technique (e.g., plagioclase $^{40}$Ar/$^{39}$Ar and phosphate U-Pb) dating campaign centred on LL-chondrite to test if an age concentration is defined around 4.2 Ga based on the two $^{40}$Ar/$^{39}$Ar ages obtained in this study.

## References


1. Jourdan F, *et al.* (2017) Collisional history of asteroid Itokawa. *Geology* 45(9):819-822.
2. Nakamura T, *et al.* (2011) Itokawa dust particles: a direct link between S-type asteroids and ordinary chondrites. *Science* 333(6046):1113-1116.
3. Rickard WD, *et al.* (2020) Novel applications of FIB-SEM-based ToF-SIMS in atom probe tomography workflows. *Microscopy and Microanalysis*.
4. Barrat J-A, *et al.* (2011) Possible fluid–rock interactions on differentiated asteroids recorded in eucritic meteorites. *Geochim Cosmochim Ac* 75(13):3839-3852.
5. Ware B & Jourdan F (2018) 40Ar/39Ar geochronology of terrestrial pyroxene. *Geochim Cosmochim Ac* 230:112-136.
6. Jourdan F, Kennedy T, Benedix GK, Eroglu E, & Mayer C (2020) Timing of the magmatic activity and upper crustal cooling of differentiated asteroid 4 Vesta. *Geochim Cosmochim Ac* 273:205-225.
7. Cassata WS, Renne PR, & Shuster DL (2011) Argon diffusion in pyroxenes: Implications for thermochronometry and mantle degassing. *Earth Planet Sc Lett* 304(3-4):407-416.
8. Cassata WS, Shuster DL, Renne PR, & Weiss BP (2010) Evidence for shock heating and constraints on Martian surface temperatures revealed by Ar-40/Ar-39 thermochronometry of Martian meteorites. *Geochim Cosmochim Ac* 74(23):6900-6920.
9. Jourdan F, Benedix G, Eroglu E, Bland PA, & Bouvier A (2014) 40Ar/39Ar impact ages and time–temperature argon diffusion history of the Bunburra Rockhole anomalous basaltic achondrite. *Geochim Cosmochim Ac* 140:391-409.

10. Kennedy T, Jourdan F, Bevan AWR, Mary Gee MA, & Frew A (2013) Impact history of the HED parent body(ies) clarified by new 40Ar/39Ar analyses of four HED meteorites and one anomalous basaltic achondrite. *Geochim Cosmochim Ac* 115:162-182.
11. Boehnke P, Harrison TM, Heizler MT, & Warren PH (2016) A model for meteoritic and lunar 40Ar/39Ar age spectra: Addressing the conundrum of multi-activation energies. *Earth Planet Sc Lett* 453:267-275.
12. Weirich J, Isachsen C, Johnson J, & Swindle T (2012) Variability of diffusion of argon in albite, pyroxene, and olivine in shocked and unshocked samples. *Geochim Cosmochim Ac* 77:546-560.
13. Wakita S, Nakamura T, Ikeda T, & Yurimoto H (2014) Thermal modeling for a parent body of Itokawa. *Meteorit Planet Sci* 49(2):228-236.
14. Gail H-P & Trieloff M (2019) Thermal history modelling of the L chondrite parent body. *Astronomy and astrophysics.* 628:A77.
15. Jourdan F & Eroglu E (2017) 40Ar/39Ar and (U-Th)/He model age signatures of elusive Mercurian and Venusian meteorites. *Meteorit Planet Sci* 52(5):884-905.
16. Cassata WS & Renne PR (2013) Systematic variations of argon diffusion in feldspars and implications for thermochronometry. *Geochim Cosmochim Ac* 112:251-287.
17. McDougall I & Harrison TM (1999) *Geochronology and thermochronology by the 40Ar/39Ar method* (Oxford University Press, Oxford, New York) p 269.
18. Humayun M & Koeberl C (2004) Potassium isotopic composition of Australasian tektites. *Meteorit Planet Sci* 39(9):1509-1516.
19. Leverington DW (2007) Was the Mangala Valles system incised by volcanic flows? *Journal of Geophysical Research: Planets* 112(E11).
20. Mitchell KL (2005) Coupled conduit flow and shape in explosive volcanic eruptions. *Journal of volcanology and geothermal research* 143(1-3):187-203.
21. Lucas MP*, et al.* (2020) Evidence for early fragmentation-reassembly of ordinary chondrite (H, L, and LL) parent bodies from REE-in-two-pyroxene thermometry. *Geochim Cosmochim Ac* 290:366-390.
22. Nagao K*, et al.* (2011) Irradiation history of Itokawa regolith material deduced from noble gases in the Hayabusa samples. *Science* 333(6046):1128-1131.
23. Fritz J, Greshake A, & Fernandes VA (2017) Revising the shock classification of meteorites. *Meteorit Planet Sci* 52(6):1216-1232.
24. Schmitt RT (2000) Shock experiments with the H6 chondrite Kernouve: Pressure calibration of microscopic shock effects. *Meteoritics and Planetary Science* 35(3):545-560.
25. Bland P*, et al.* (2014) Pressure–temperature evolution of primordial solar system solids during impact-induced compaction. *Nature communications* 5(1):1-13.
26. Terada K*, et al.* (2018) Thermal and impact histories of 25143 Itokawa recorded in Hayabusa particles. *Scientific Reports* 8(1):11806.
27. Park J*, et al.* (2015) 40Ar/39Ar age of material returned from asteroid 25143 Itokawa. *Meteoritics and Planetary Science*.
28. VanLaningham S & Mark DF (2011) Step heating of 40Ar/39Ar standard mineral mixtures: investigation of a fine-grained bulk sediment provenance tool. *Geochim Cosmochim Ac* 75(9):2324-2335.
29. Jourdan F*, et al.* (2021) End of magmatism in the upper crust of asteroid 4 Vesta. *Meteorit Planet Sci* 56(3):619-641.
30. Okada T*, et al.* (2006) Thermal radiometry of asteroid itokawa by the XRS onboard Hayabusa. *37th Annual Lunar and Planetary Science Conference*.

31. Yano H*, et al.* (2006) Touchdown of the Hayabusa spacecraft at the Muses Sea on Itokawa. *Science* 312(5778):1350-1353.
32. Bogard DD (2011) K-Ar ages of meteorites: Clues to parent-body thermal histories. *Chem Erde-Geochem* 71(3):207-226.
33. Dixon E, Bogard D, Garrison D, & Rubin A (2004) 39Ar-40Ar evidence for early impact events on the LL parent body. *Geochim Cosmochim Ac* 68(18):3779-3790.
34. Jourdan F (2012) The Ar-40/Ar-39 dating technique applied to planetary sciences and terrestrial impacts. *Aust J Earth Sci* 59(2):199-224.
35. Kennedy T, Jourdan F, Eroglu E, & Mayers C (2019) Bombardment history of asteroid 4 Vesta recorded by brecciated eucrites: Large impact event clusters at 4.50 Ga and discreet bombardment until 3.47 Ga. *Geochim Cosmochim Ac* 260:99-123.
36. Nemchin AA*, et al.* (2020) Ages of lunar impact breccias: Limits for timing of the Imbrium impact. *Geochemistry*:125683.
37. Jourdan F, Renne P, & Reimold W (2009) An appraisal of the ages of terrestrial impact structures. *Earth Planet Sc Lett* 286(1-2):1-13.
38. Ash RD, Gilmour JD, Turner G, Bridges J, & Hutchison R (1994) The chronology of ordinary chondrites by laser Ar-Ar and I-Xe. *Meteoritics* 29:439-440.
39. Swindle TD, Kring DA, & Weirich JR (2014) 40Ar/39Ar ages of impacts involving ordinary chondrite meteorites. *Advances in 40Ar/39Ar Dating: from Archaeology to Planetary Sciences*, eds Jourdan F, Mark DF, & Verati C (Geological Society, London), Vol 378, pp 333-347.
40. Jourdan F, Andreoli MAG, McDonald I, & Maier WD (2010) 40Ar/39Ar thermochronology of the fossil LL6-chondrite from the Morokweng crater, South Africa. *Geochim Cosmochim Ac* 74(5):1734-1747.

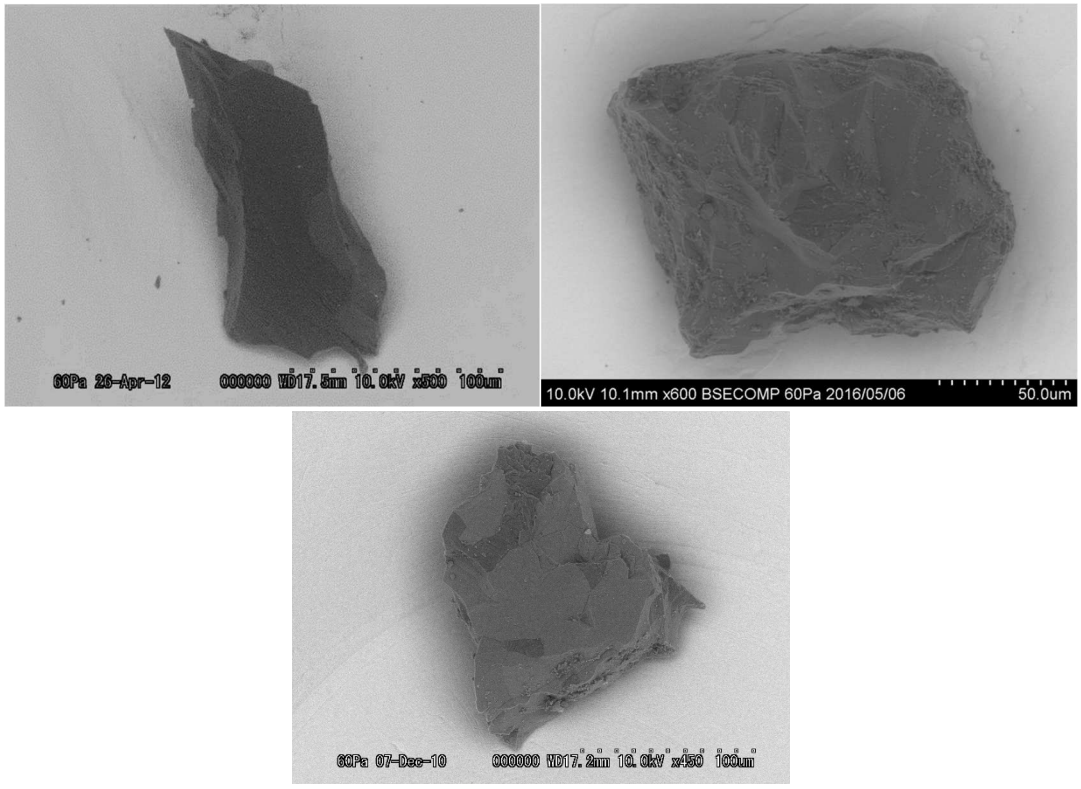


***Fig. S1****: SEM (Secondary Electron Microscope) images of particles #0059 (top left) and #0288 (top right), and #0010 (lower centre) prior to being embedded in epoxy. Images courtesy of JAXA.*

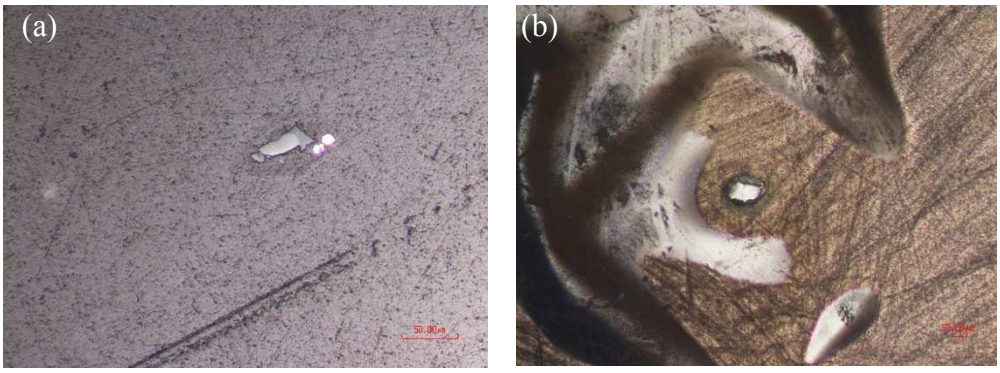


***Fig. S2**: Particles #0059 and #0288 embedded in epoxy*

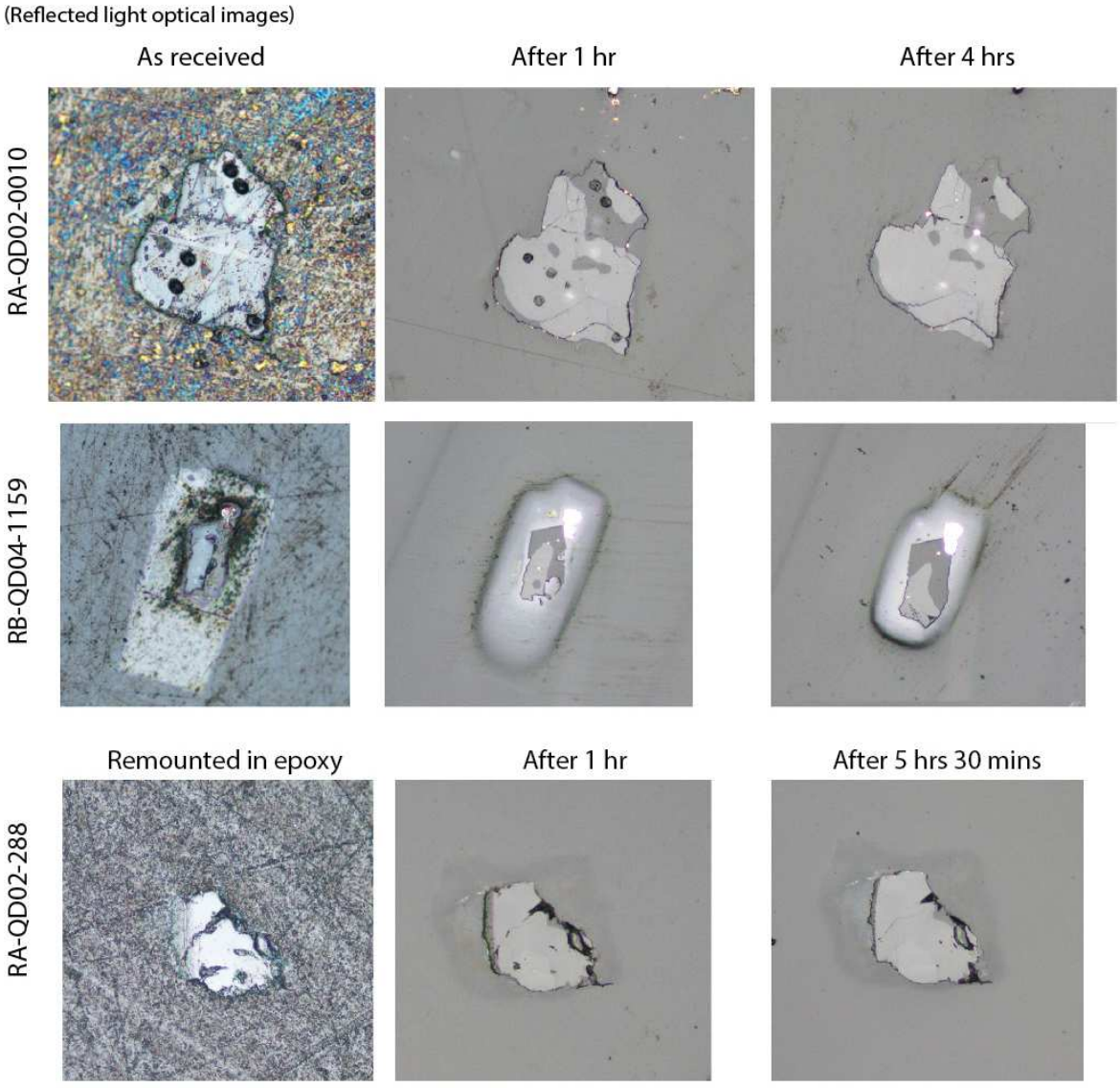

***Fig. S3**: Reflected light optical photomicrographs of the surfaces of the three particles as received at Curtin University (left), after 1h (middle) and 4h / 5h30 (right) of polishing with 0.06 µm colloidal silica to remove the prexisting carbon-coating and mechanical polishing damage prior to SEM, EBSD and ToF-SIMS analysis at Curtin University.*

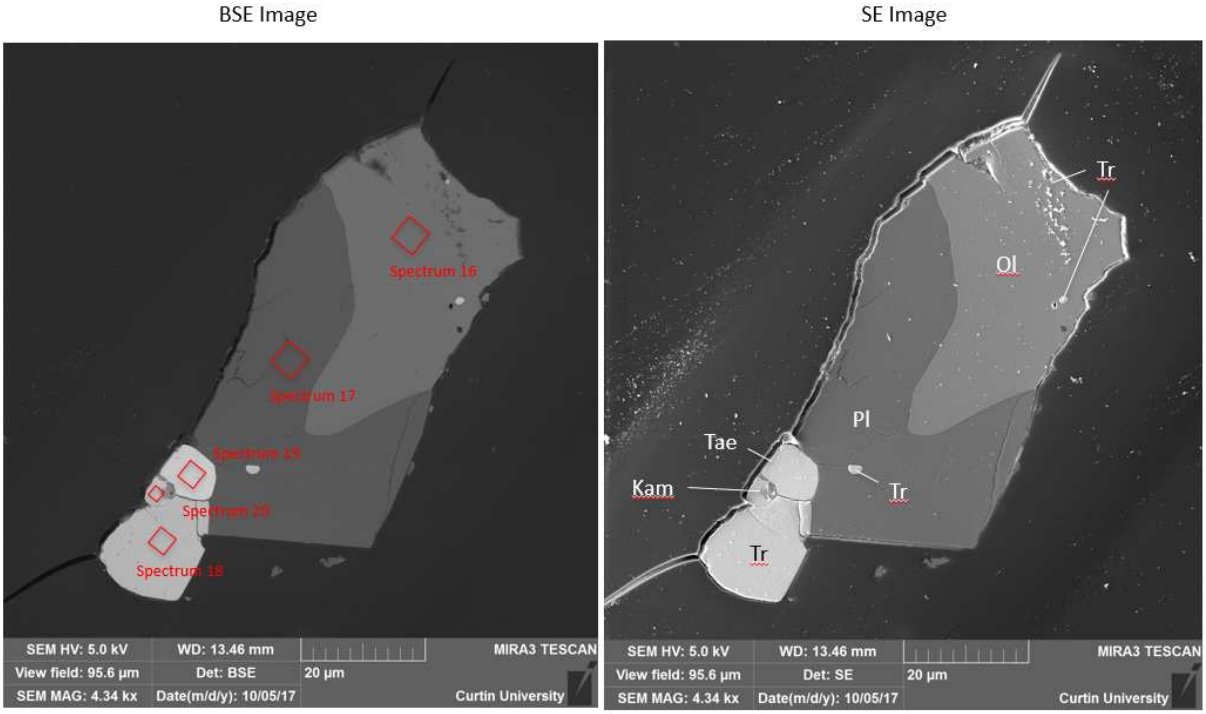


***Fig. S4**: BSE and SE images of particle #0059 after polishing at Curtin University. Ol: olivine, Pl: plagioclase, Tr: troilite, Ta: Taenite, Kam: Kamacite. Red boxes indicate areas covered by EDX spectral analysis locations corresponding to the phase composition data presented in Table S1.*

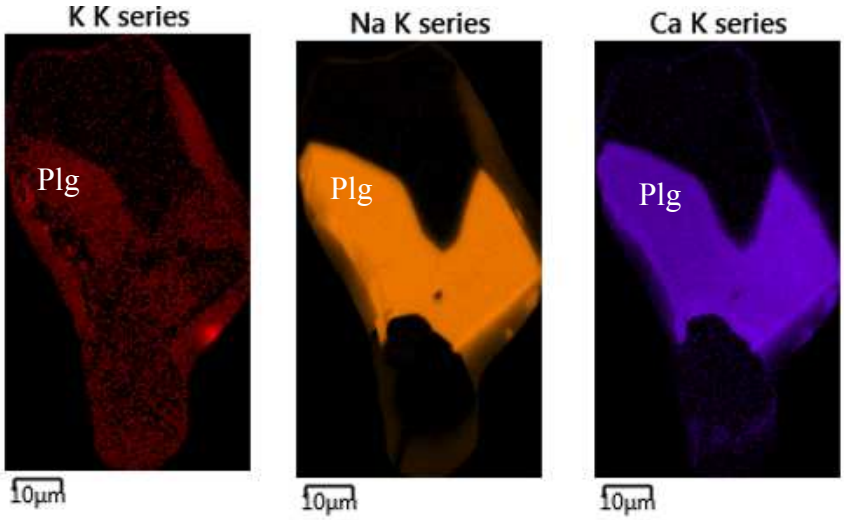


***Fig. S5**: EDX element maps for K, Na and Ca showing the homogeneous chemical composition of plagioclase in particle #0010.*

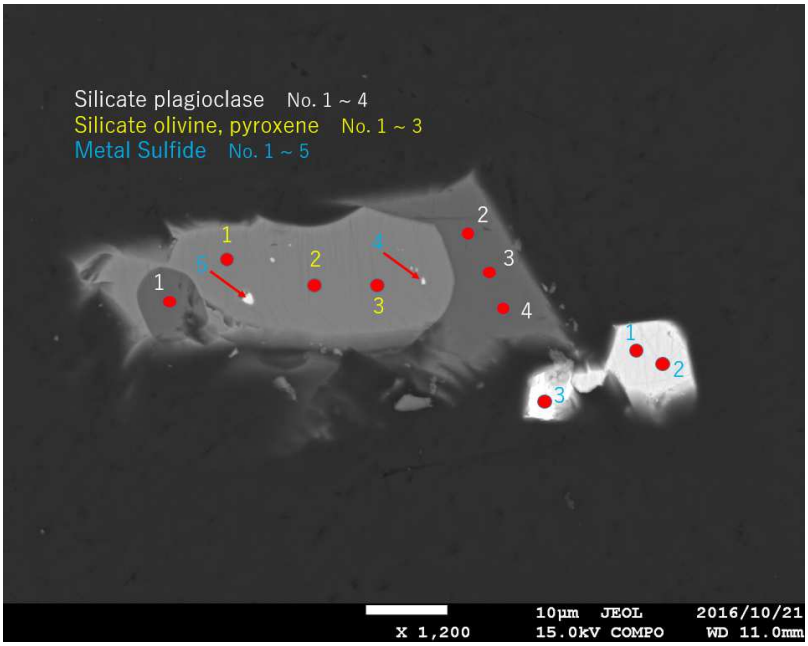


***Fig. S6****: BSE image of particle #0059 showing the location analysed by EMPA at* Tohoku University, Japan

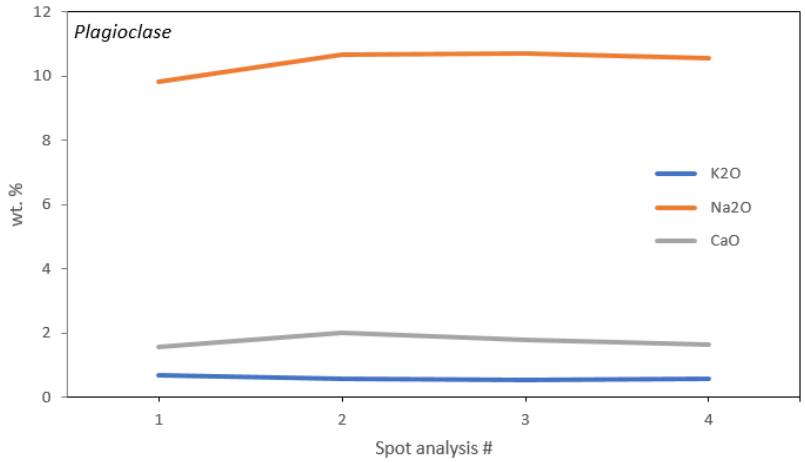


***Fig. S7****: EMPA measurements of $K_2O$, CaO and Na2O concentration of plagioclase crystals shown in Fig. S6 and indicating a homogenous composition for plagioclase.*

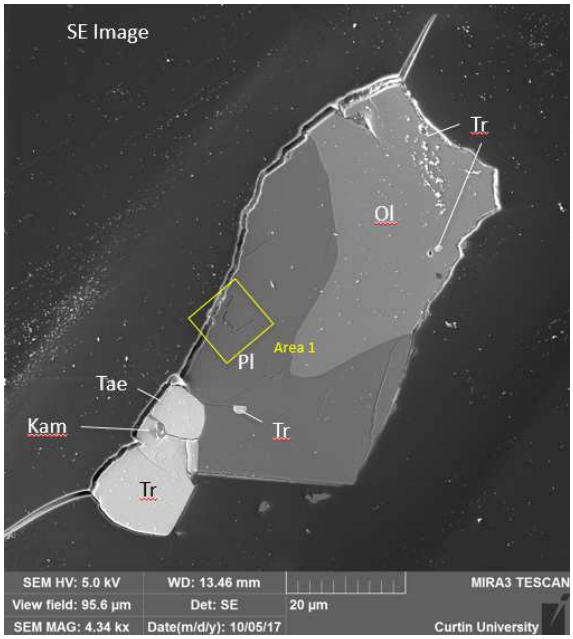


***Fig. S8****: SE image showing the area targeted for Time-of-flight secondary ion mass spectrometry (ToF-SIMS) analysis in particle #0059. The area 1 (10 x 10 µm) was chosen to assess the distribution of K in plagioclase and test the presence of K-feldspar exsolutions.*

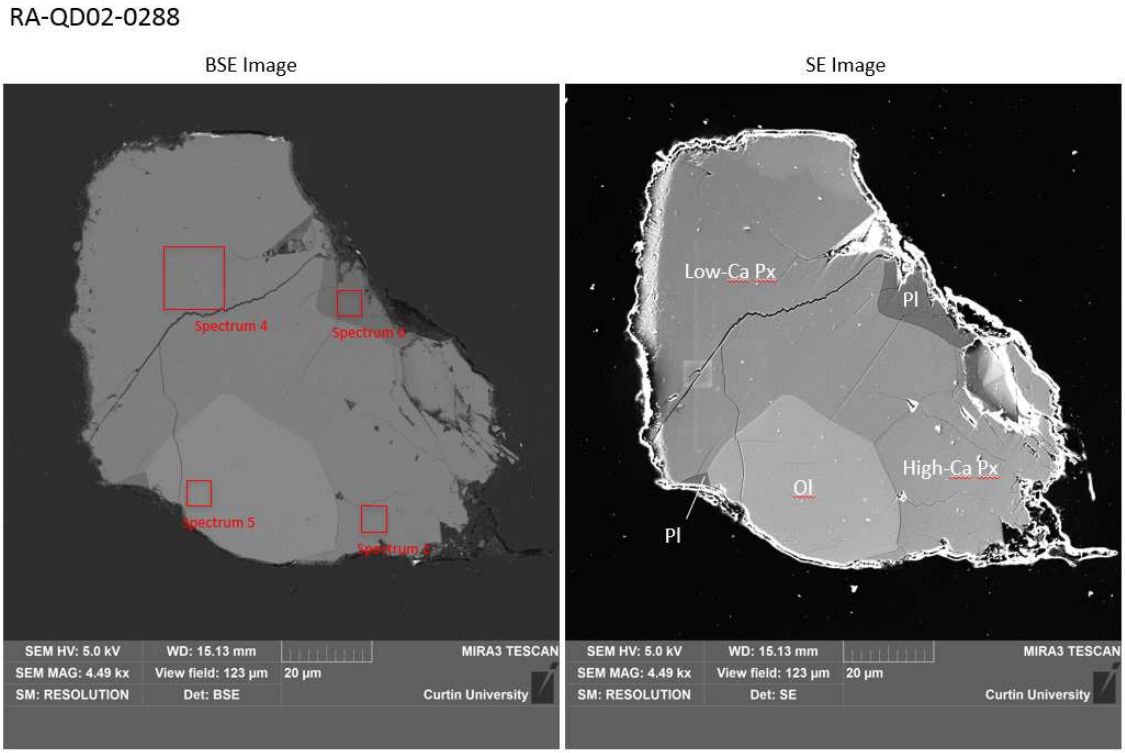


***Fig. S9****: BSE and SE images of particle #0288 after polishing at Curtin University. Ol: olivine, Pl: plagioclase, Low-Ca Px: low-Ca pyroxene, High-Ca Px: high-Ca pyroxene. Red boxes indicate areas covered by EDX spectral analysis locations corresponding to the phase composition data presented in Table S2.*

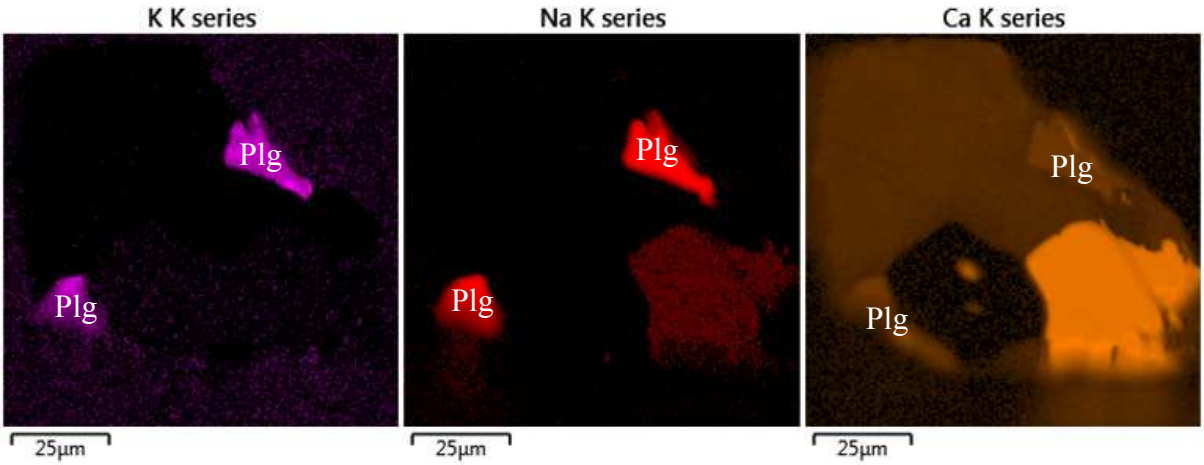


***Fig. S10**: EDX element maps for K, Na and Ca in particle #0288.*

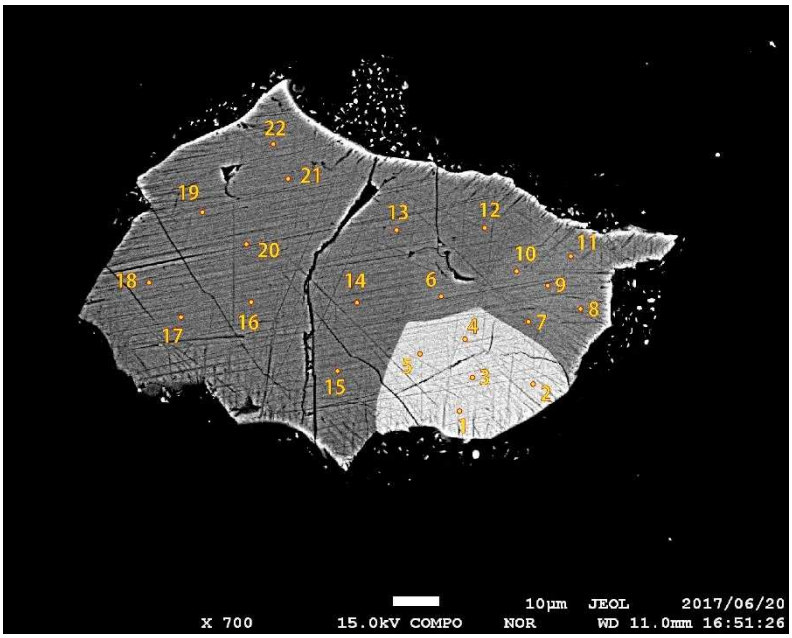


***Fig. S11**: BSE image of particle #0288 showing the location analysed by EMPA at* Tohoku *University, Japan. Note that no plagioclase was visible with the first round of polishing therefore, our analyses include only olivine (#1-5), High-Ca pyroxene (#6-11) and low-Ca pyroxene (#12-22) chemical compositions*

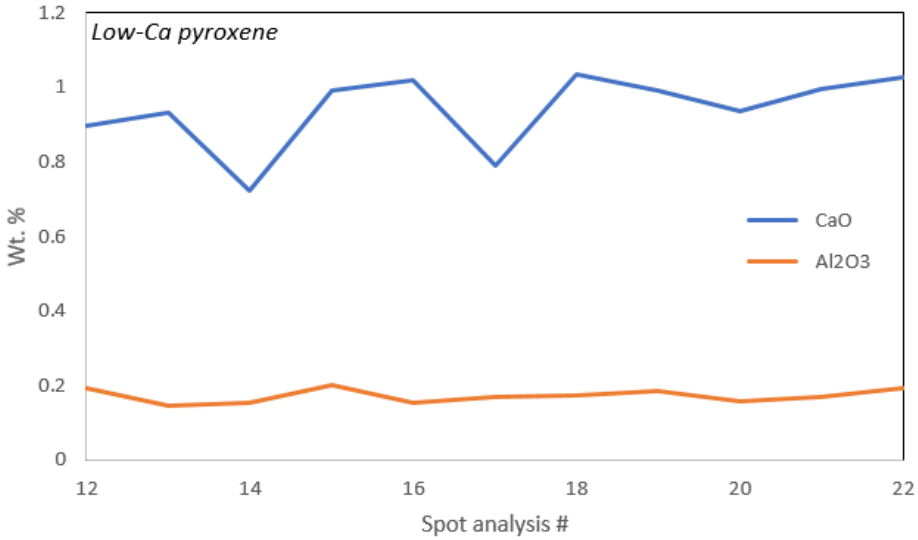


***Fig. S12**: EMPA measurements of CaO and Al2O3 concentration of Low-Ca pyroxene crystals shown in Fig. Sx and indicating a homogenous composition.*

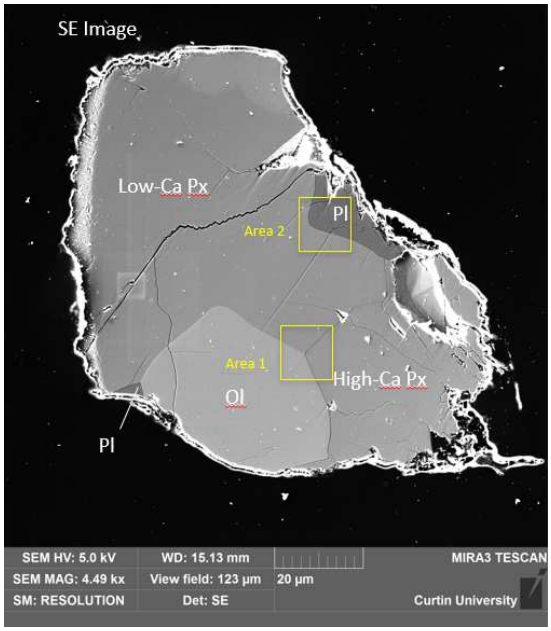


***Fig. S13**: SE image showing the two areas targeted for Time-of-flight secondary ion mass spectrometry (ToF-SIMS) analysis. Area 1: (15 x 15 µm) at the triple junction between olivine, and, high-Ca and low-Ca pyroxene. Area 2: (15 x 15 µm) at the boundary between low-Ca pyroxene and plagioclase*

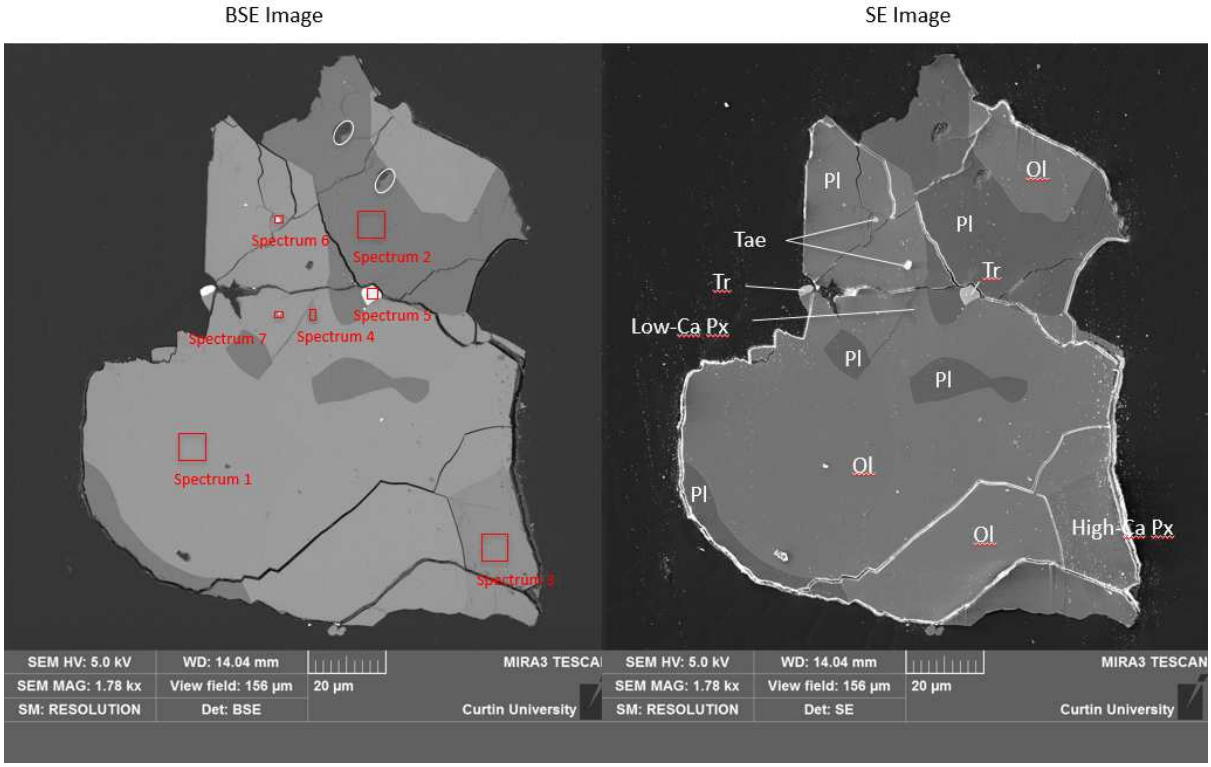


***Fig. S14****: BSE and SE images of particle #0010 after polishing at Curtin University. Ol: olivine, Pl: plagioclase, Low-Ca Px: low-Ca pyroxene, High-Ca Px: high-Ca pyroxene, Tr: troilite, Ta: taenite. Red boxes indicate areas covered by EDX spectral analysis locations corresponding to the phase composition data presented in Table S3.*

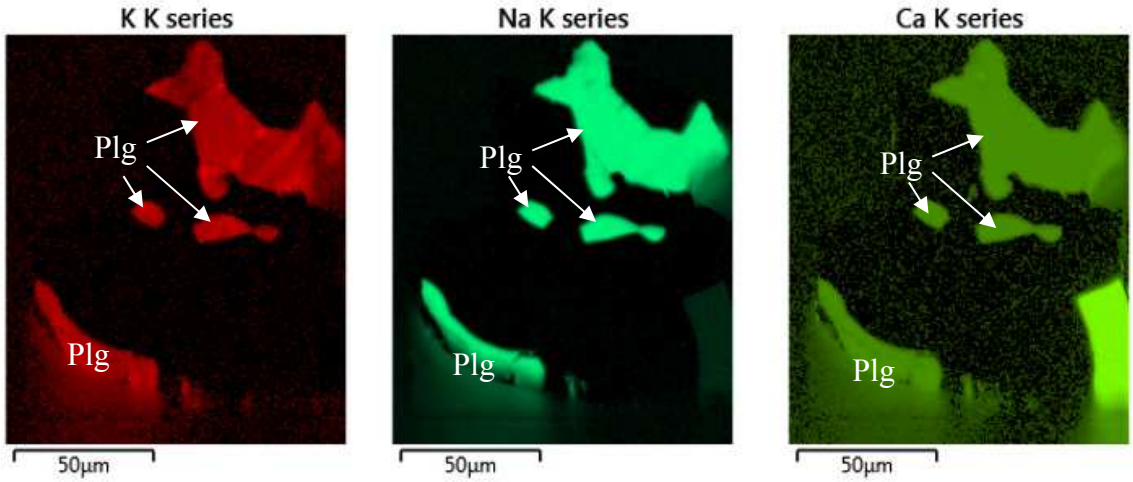


***Fig. S15****: EDX element maps for K, Na and Ca, highlighting the presence of plagioclase in particle #0010.*

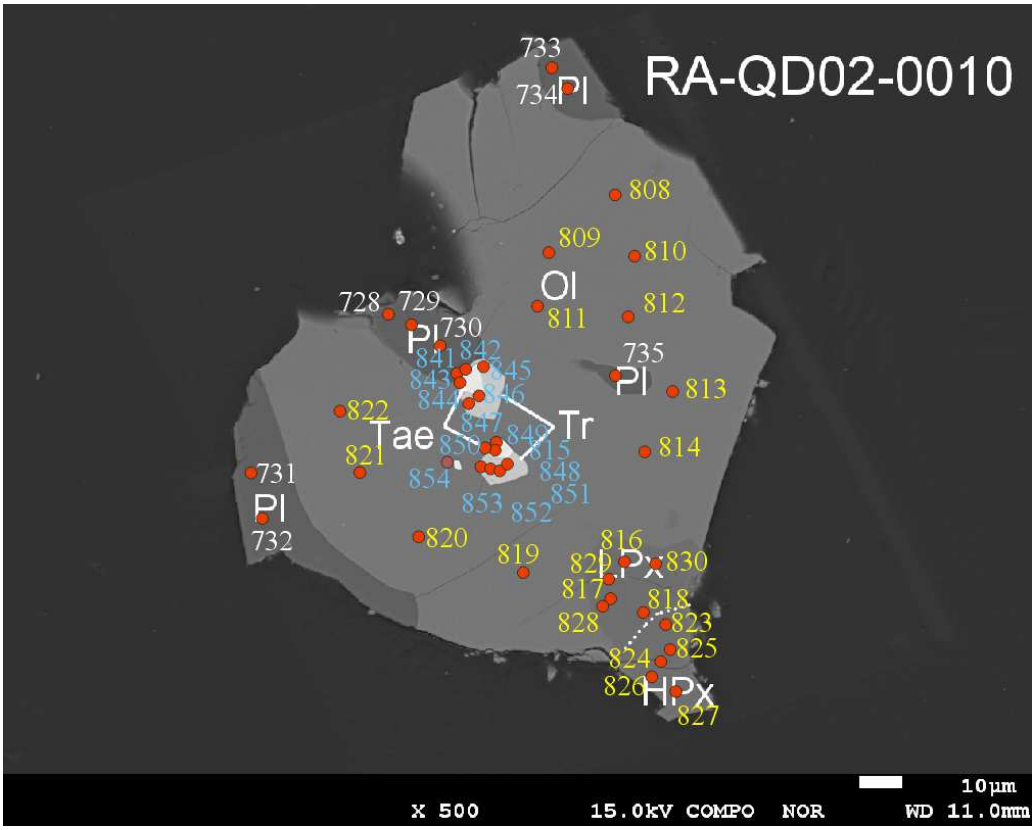


***Fig. S16**: BSE image of particle #0010 showing the location analysed by EMPA at* Tohoku *University, Japan. Analysis of plagioclase (white numbers), High-Ca pyroxene and olivine (yellow numbers) and metals (blue numbers) chemical compositions*

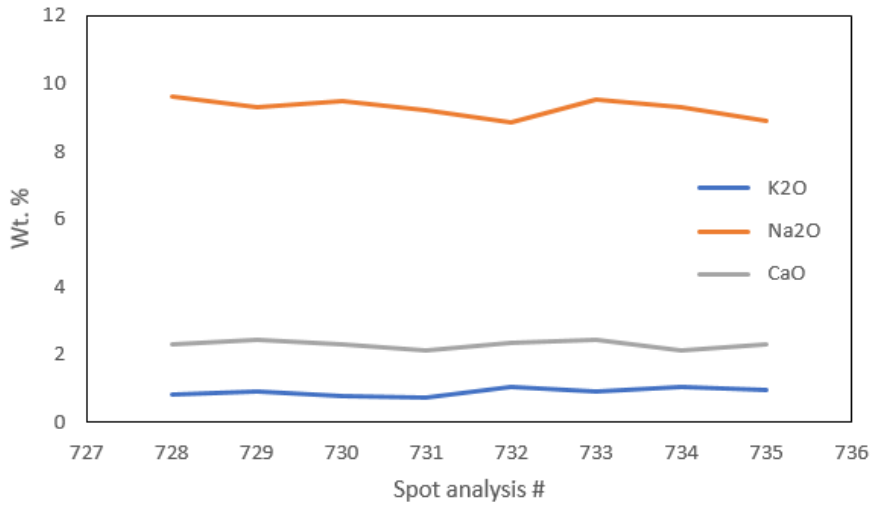


***Fig. S17**: EMPA measurements of $K_2O$, CaO and Na2O concentration of plagioclase crystals shown in Fig. S16 (indicated in white fonts) and indicating a homogenous composition for plagioclase.*

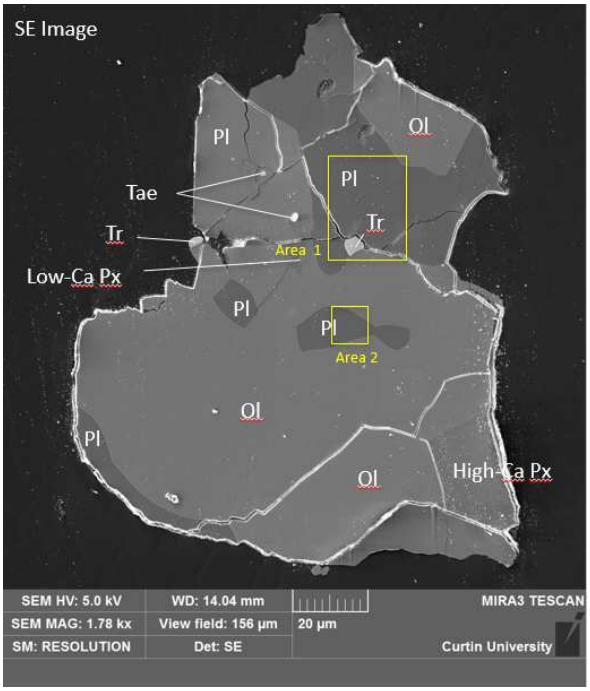


***Fig. S18**: SE image showing the two areas targeted for Time-of-flight secondary ion mass spectrometry (ToF-SIMS) analysis in particle #0010 and discussed in this study. Area 1: 20 x 40 µm to test the distribution of trace elements in plagioclase and in troilite. Area 2: 10 x 10 µm to test the distribution of trace elements in a relatively small plagioclase crystal within a large olivine crystal.*

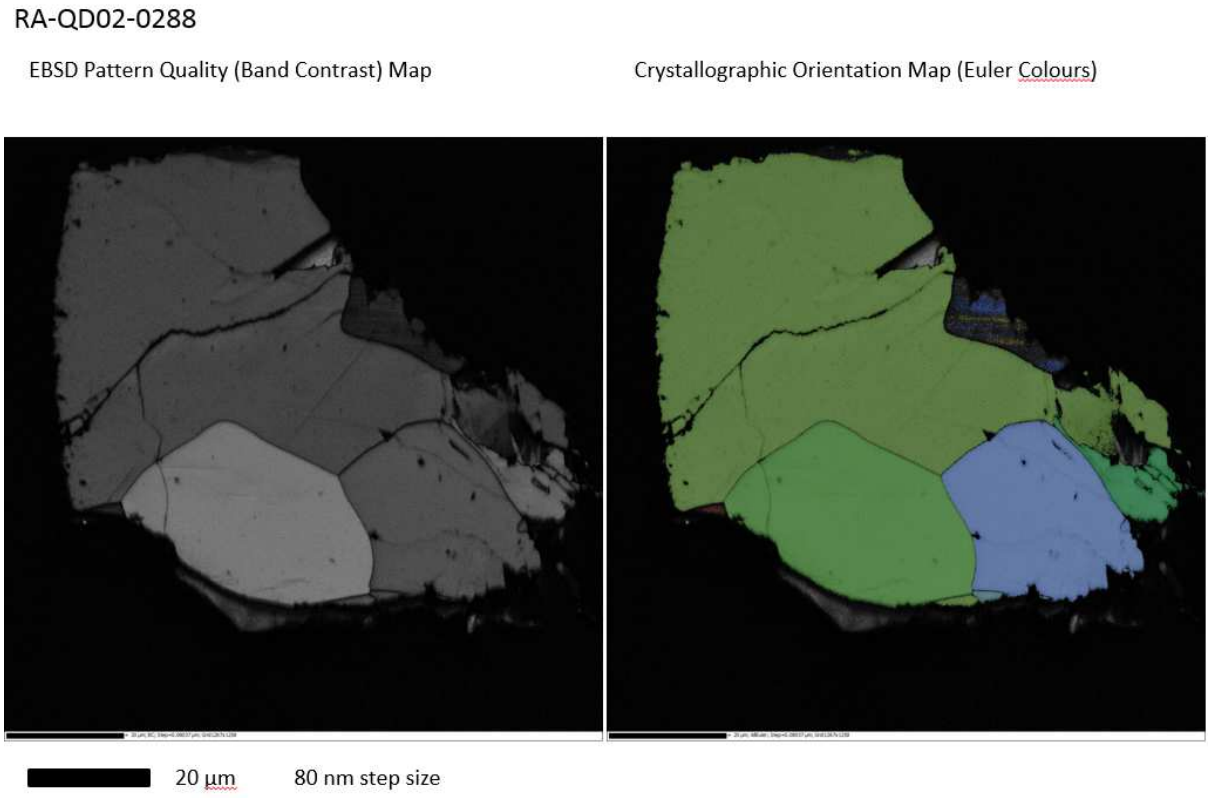

**Fig. S19**: *EBSD pattern quality (band contrast) map (left) and crystallographic orientation (all Euler colour scheme) map (right) of particle RA-QD02-0288. Both maps depict that all phases are crystalline and yield indexable EBSD patterns. Plagioclase is twinned.*

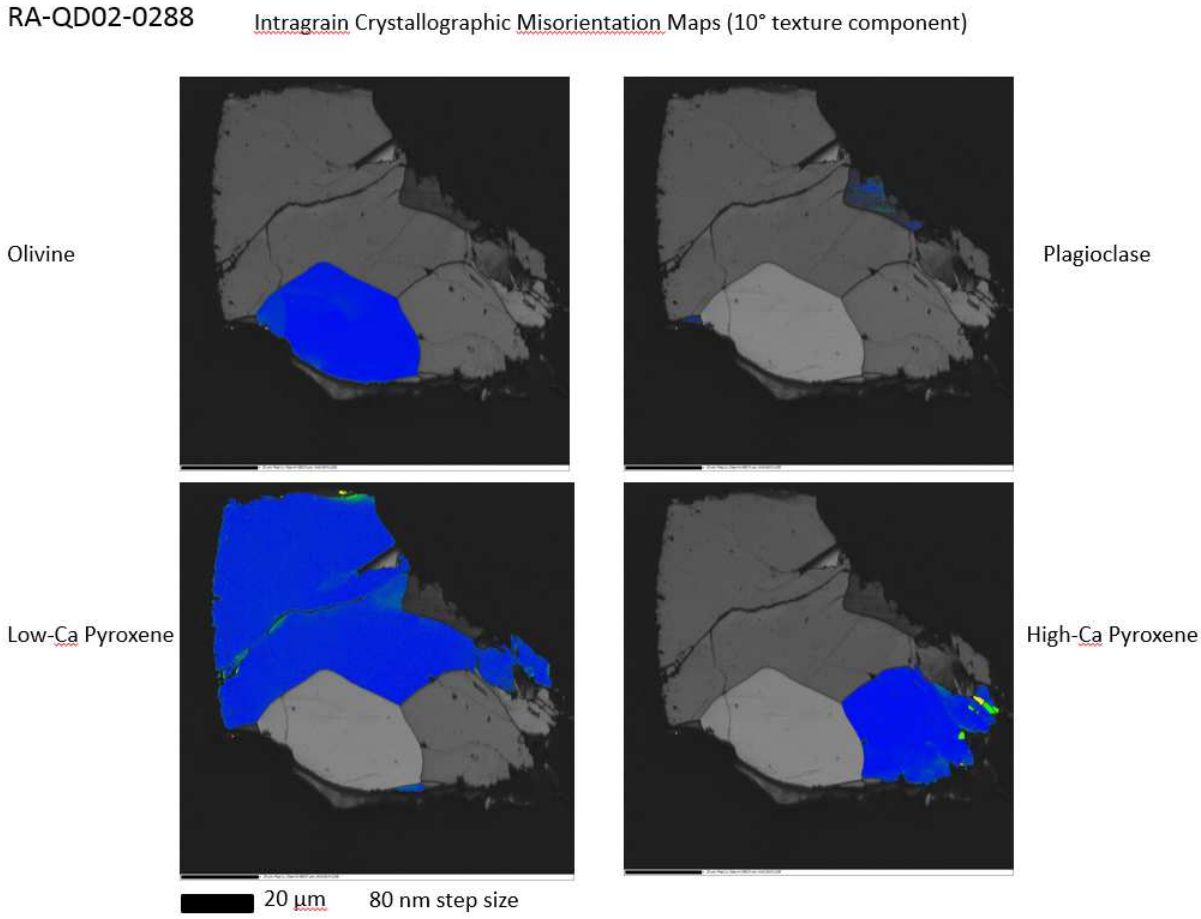


**Fig. S20**: *Intragrain crystallographic misorientation (texture component) maps of particle RA-QD02-0288. For each phase, grains are coloured for misorientation from a user-defined reference orientation (blue, 0°) up to 10° (red).*

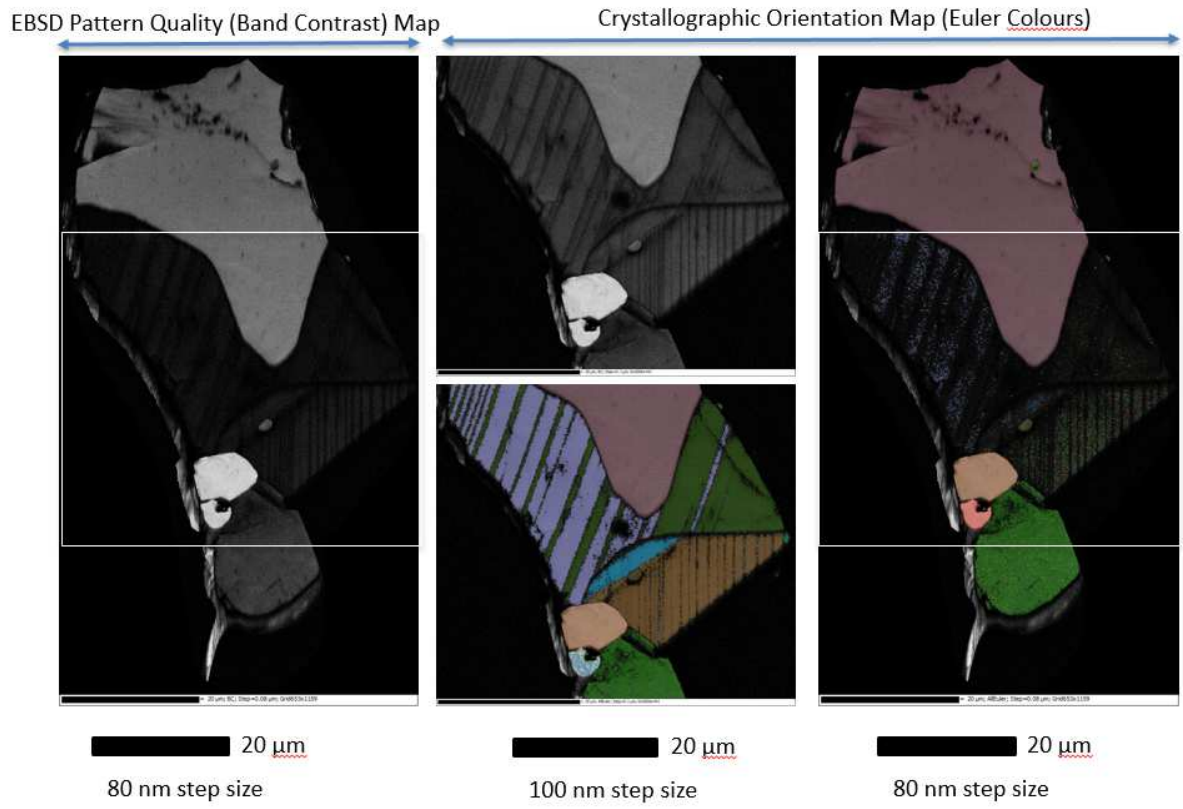


**Fig. S21***: EBSD pattern quality (band contrast) map (left, top centre) and crystallographic orientation (all Euler colour scheme) map (right, lower centre) of particle RB-QD04-0059. All maps depict that all phases are crystalline and yield indexable EBSD patterns. Plagioclase is twinned.*

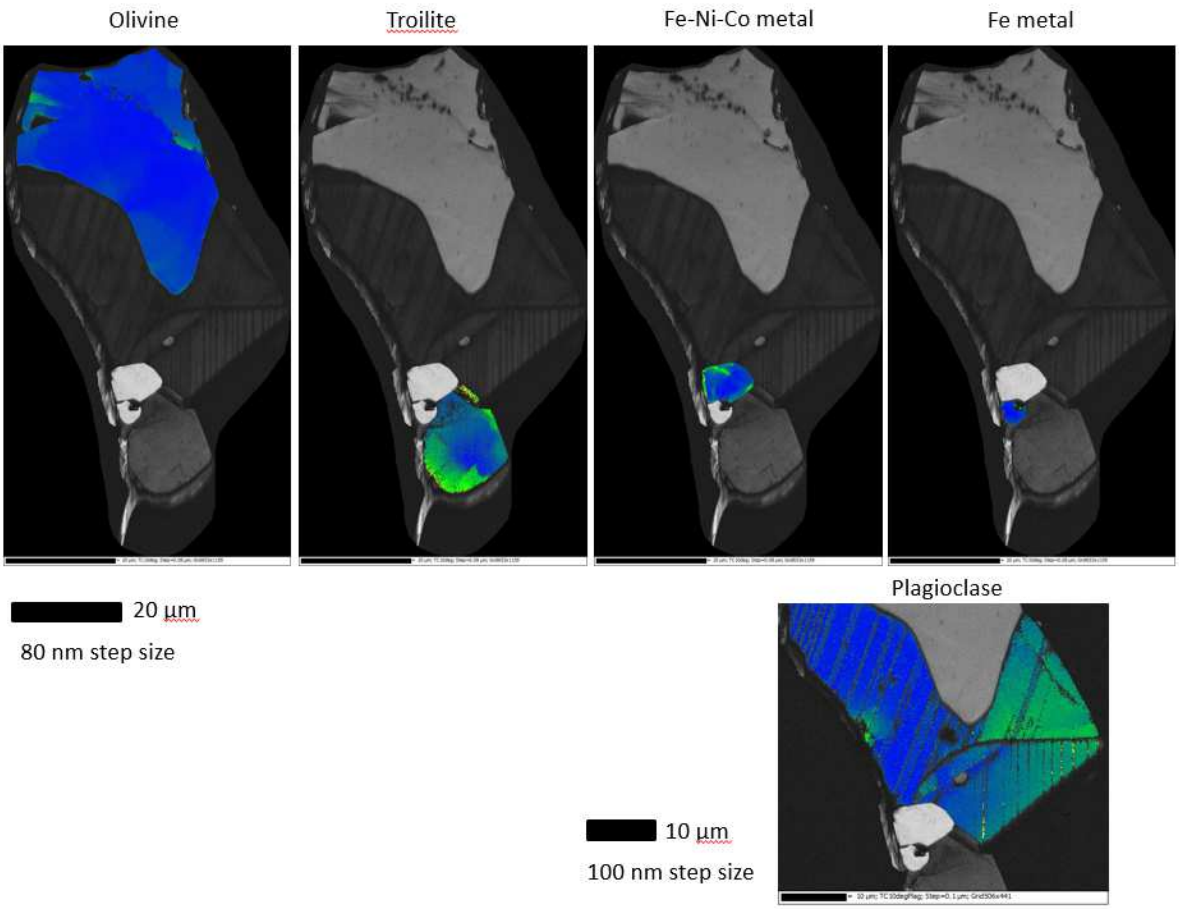


**Fig. S22**: *Intragrain crystallographic misorientation (texture component) maps of particle RB-QD04-0059. For each phase, grains are coloured for misorientation from a user-defined reference orientation (blue, 0°) up to 10° (red).*

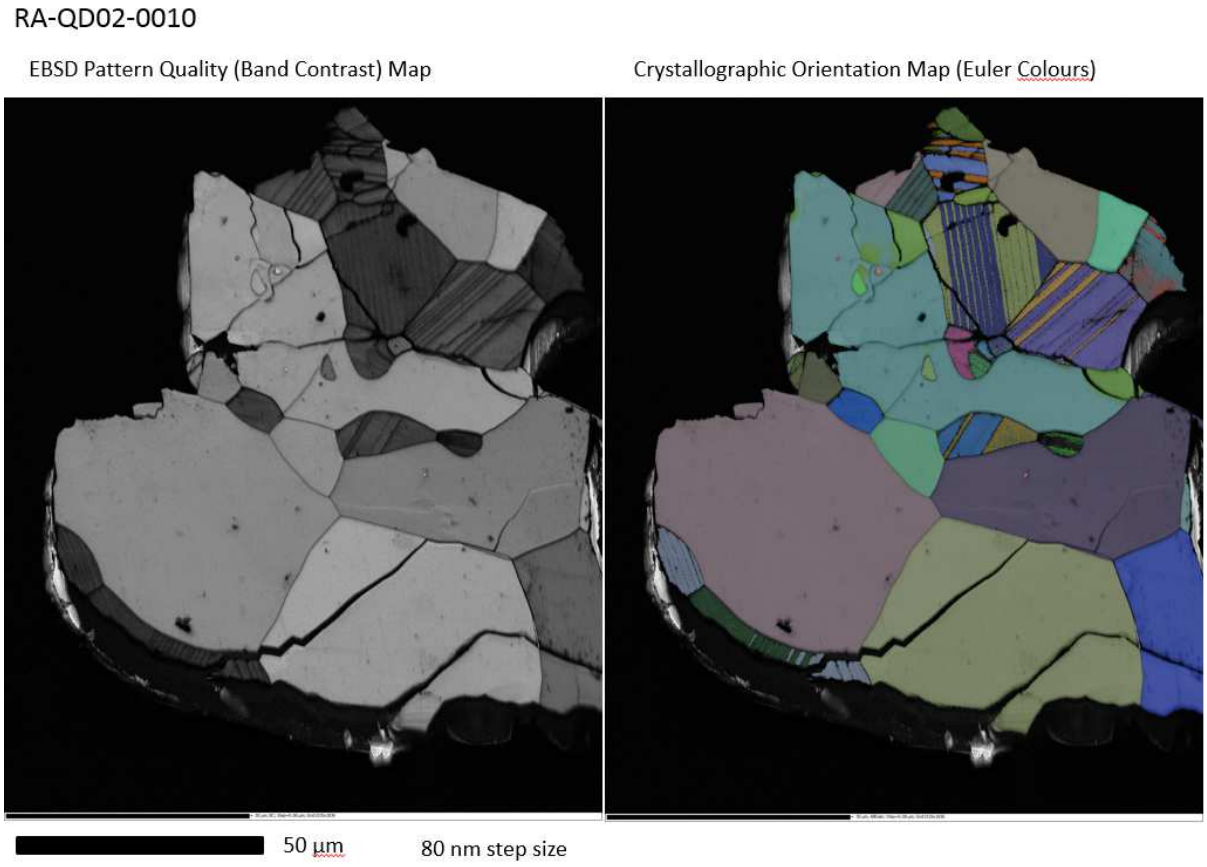


**Fig. S23***: EBSD pattern quality (band contrast) map (left) and crystallographic orientation (all Euler colour scheme) map (right) of particle RA-QD02-0010. Both maps depict that all phases are crystalline and yield indexable EBSD patterns. Plagioclase is twinned.*

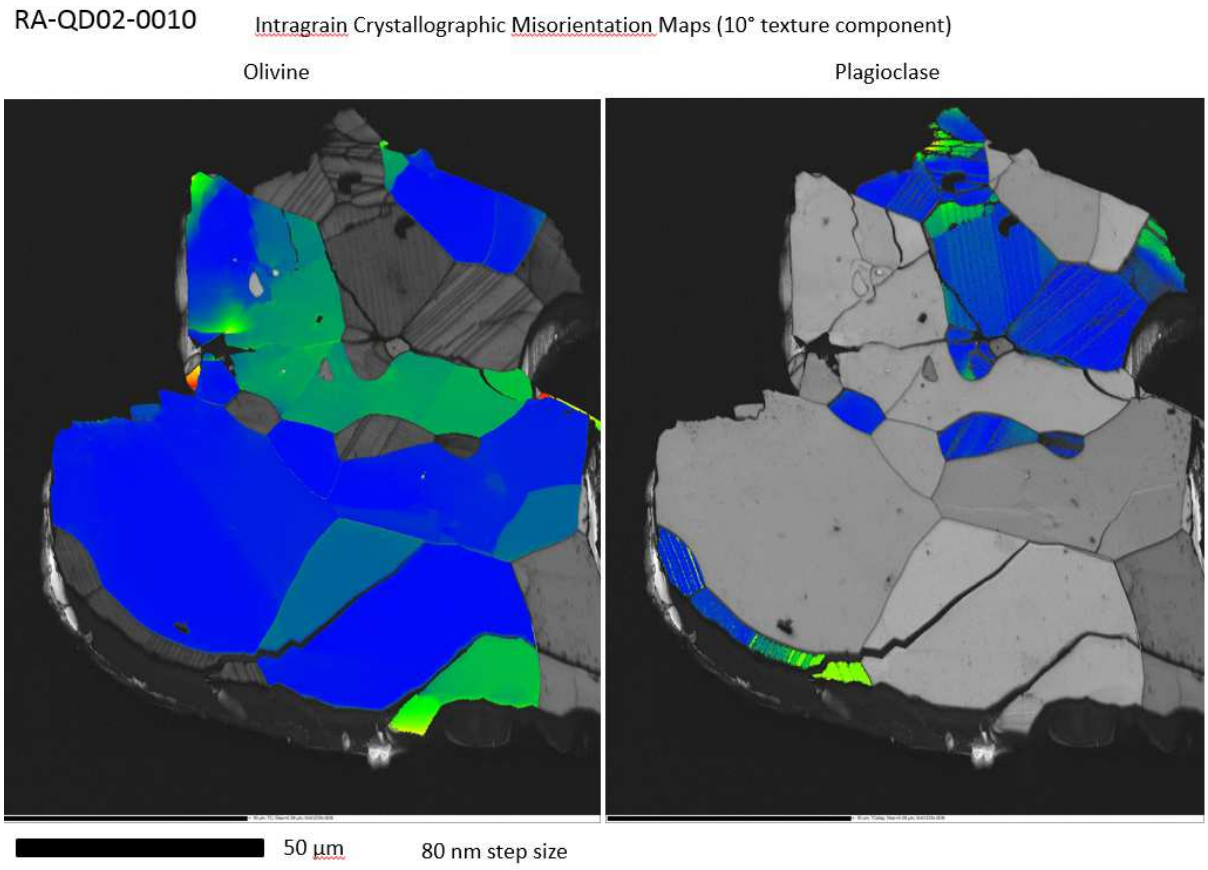


**Fig. S24**: *Intragrain crystallographic misorientation (texture component) maps of particle RA-QD02-0010. For each phase, grains are coloured for misorientation from a user-defined reference orientation (blue, 0º) up to 10º (red).*

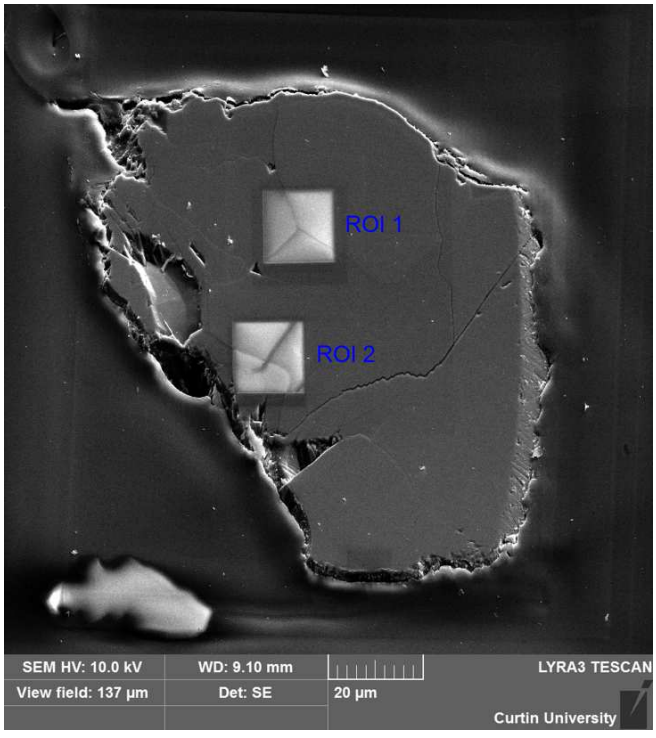

**Fig. S25**: *SEM imaging showing the two regions of interest (ROI) analysed with ToF-SIMS on particle #0288. ROI 1 is located at the triple junction between olivine and, low-Ca and high-Ca pyroxene and ROI 2 is located at the boundary between low-Ca pyroxene and plagioclase.*

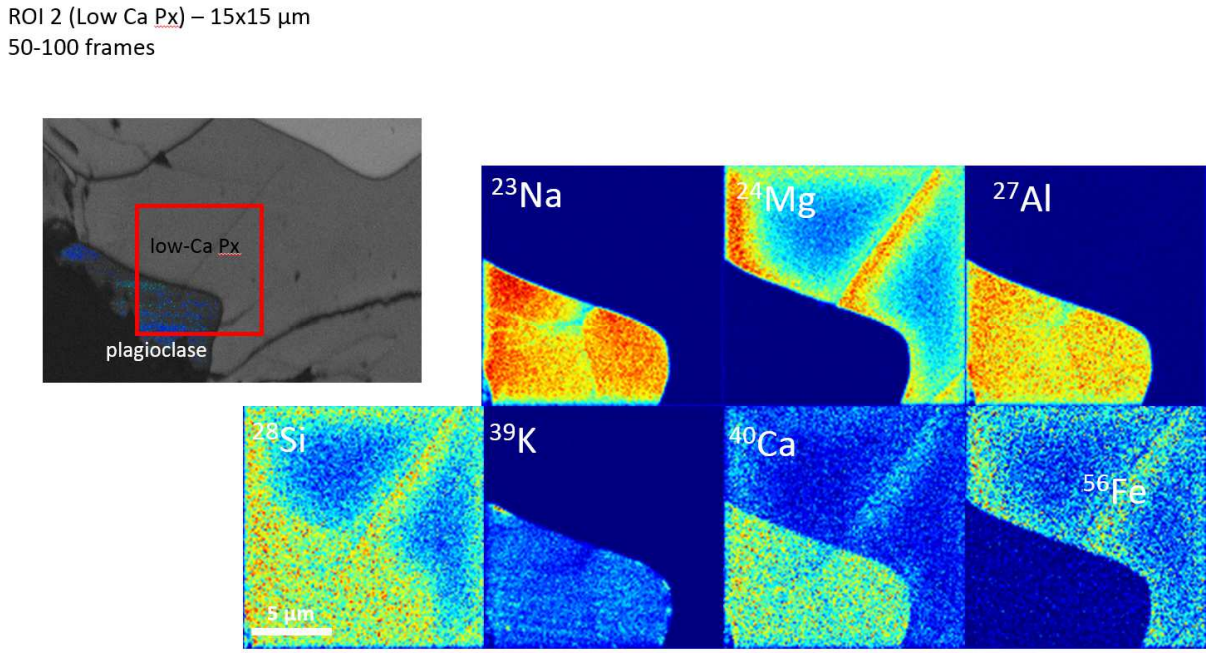


**Fig. S26**: *SEM map and FIB-ToF-SIMS maps of selected elements of low-Ca pyroxene and plagioclase from ROI 2 from particle #0288.*

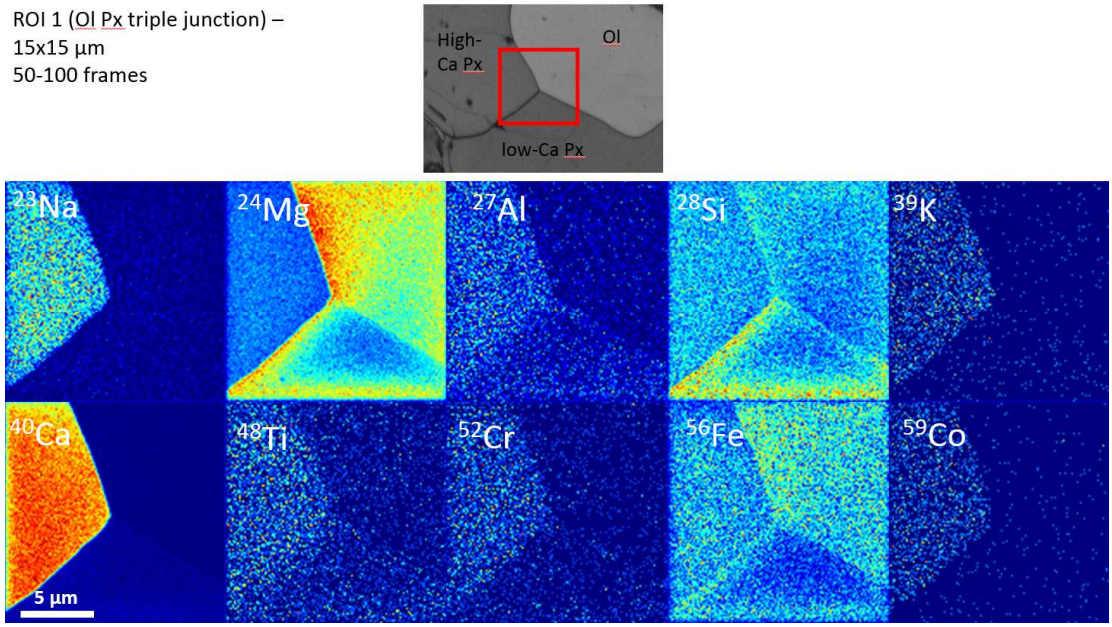


**Fig. S27**: *SEM map and FIB-ToF-SIMS maps of selected elements of high-Ca and low-Ca pyroxene and olivine from ROI 2 from particle #0288 taken at a triple junction between those phases.*

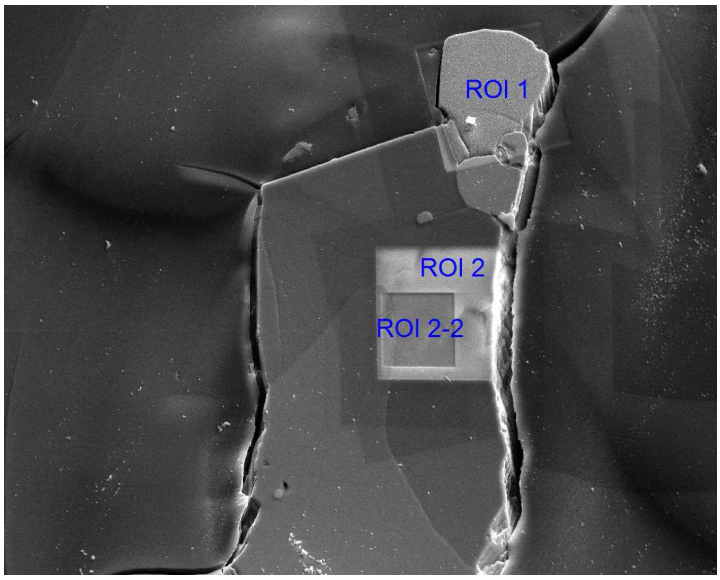


**Fig. S28***: SEM imaging showing the various regions of interest (ROI) analysed with ToF-SIMS on particle #0059. Only ROI 2 will be presented in this study.*

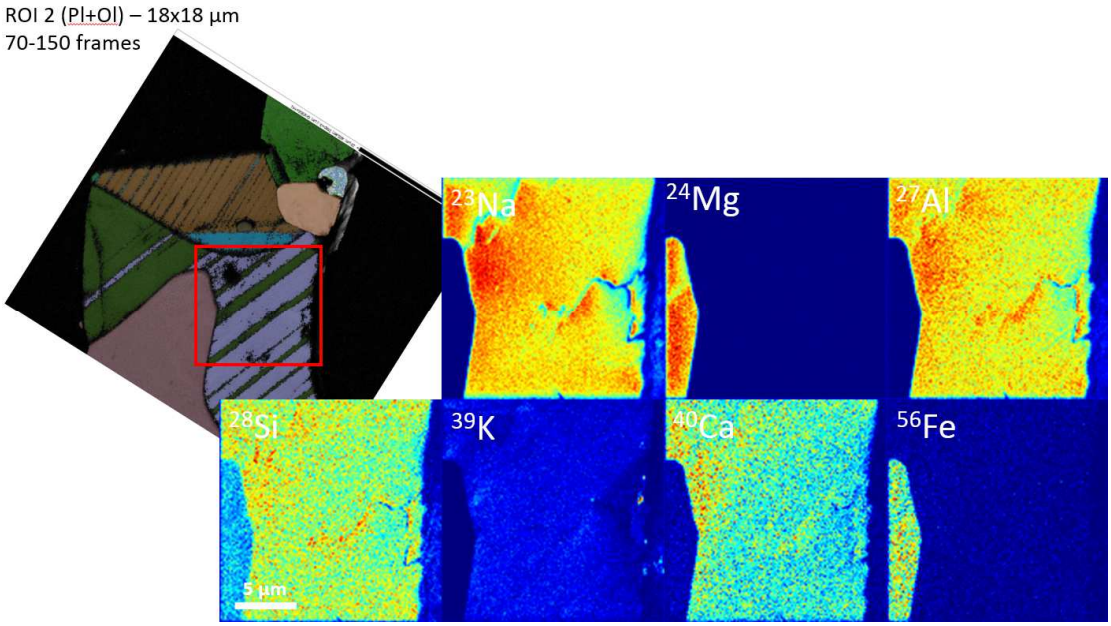


**Fig. S29***: EBSD map (all euler) and FIB-ToF-SIMS maps of selected elements from specific ROIs of plagioclase from particle #0059.*

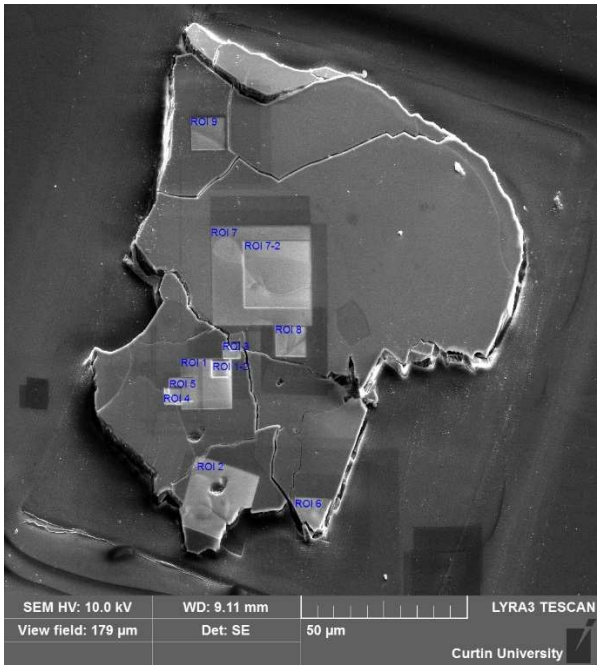


**Fig. S30***: SEM imaging showing the various regions of interest (ROI) analysed with ToF-SIMS on particle #0010. Not all data are shown in this study and chemical maps of olivine and low-Ca and high-Ca pyroxene will be presented elsewhere as these are not relevant for the present discussion.*

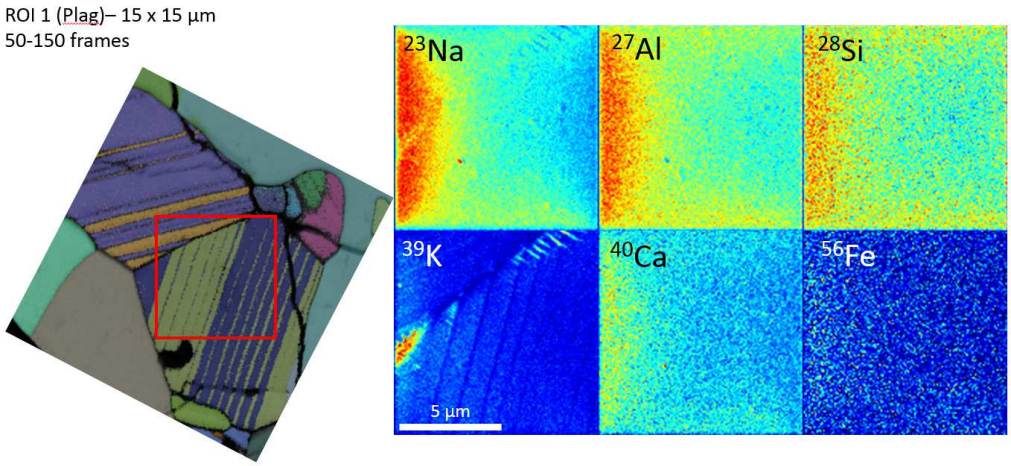


---

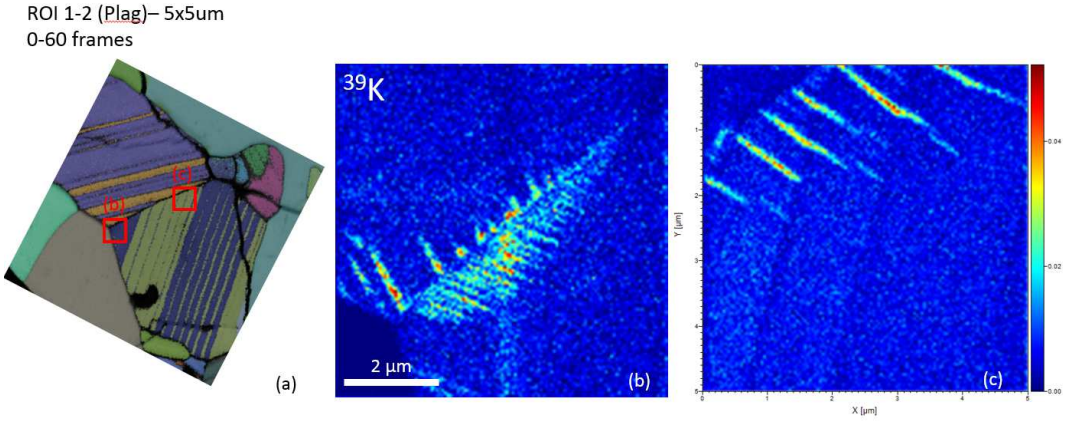

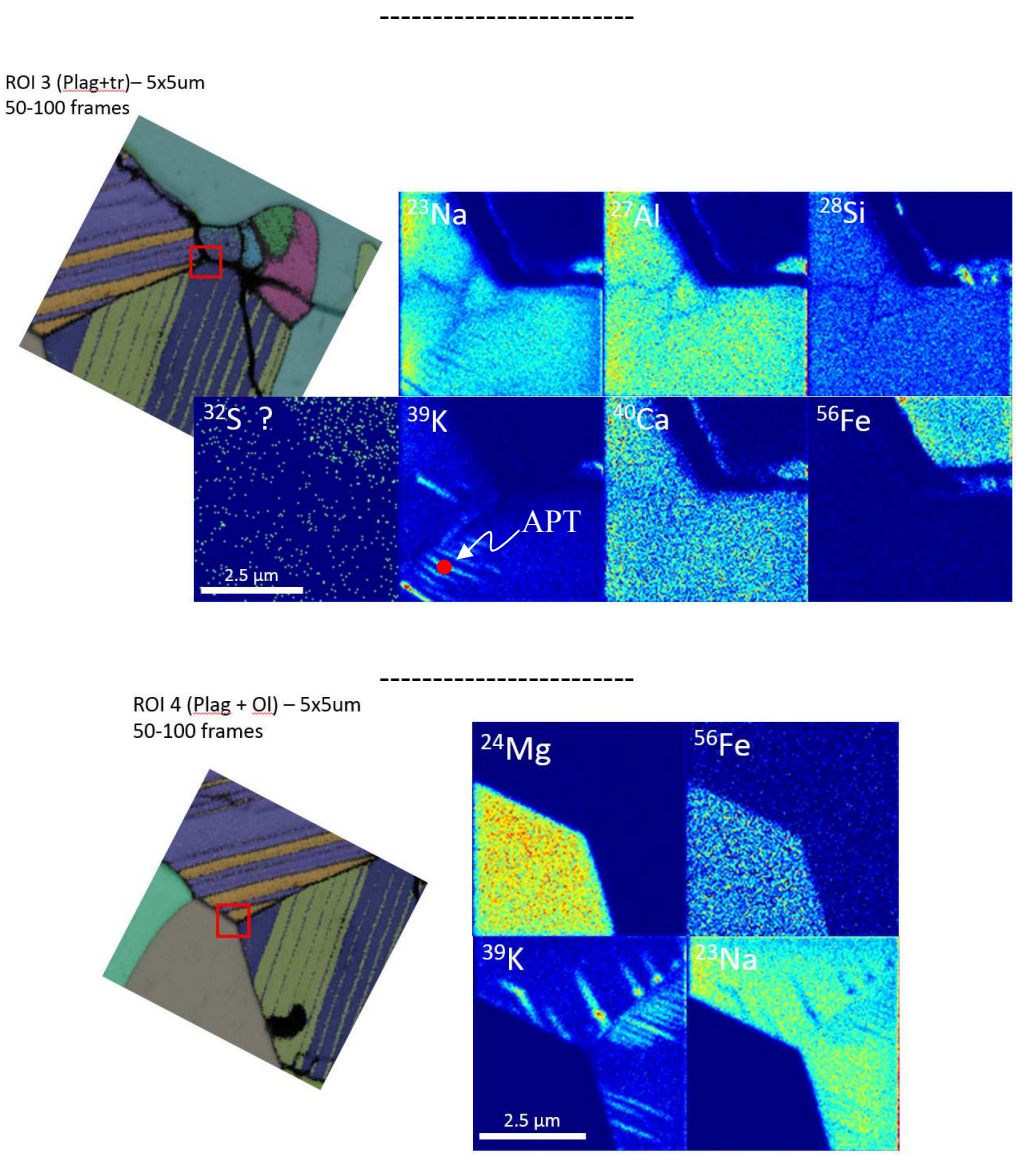


**Fig. S31**: *EBSD map (all euler) and FIB-ToF-SIMS maps of selected elements from specific ROIs of plagioclase from particle #0010. ROI numbers refers to ROI map on Fig. S30. Map dimensions and numbers of frame are indicated for each ROI. (b) and (c) in ROI 2 are FIB-ToF-SIMS maps ($^{39}K$ intensity maps displayed) from selected areas of a plagioclase crystal showing the abundant K-feldspar exsolutions* (cf. Fig. 6 from 3). *The red spot in ROI 3 indicate the location of the atom probe tomography measurements (cf. Fig. 34).*

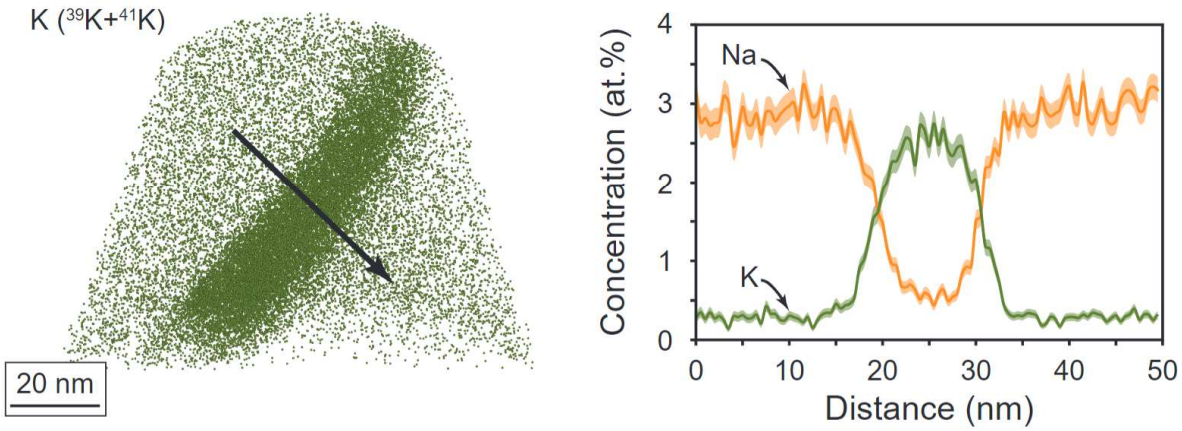


**Fig. S32**: *Atom probe tomography results from particle #0010 showing the distribution map of K atoms (left) and associated atomic concentration of K and Na (right) over the cross section indicated by the black arrow. The location of the APT measurement is indicated in Fig. S31 (ROI 3)*

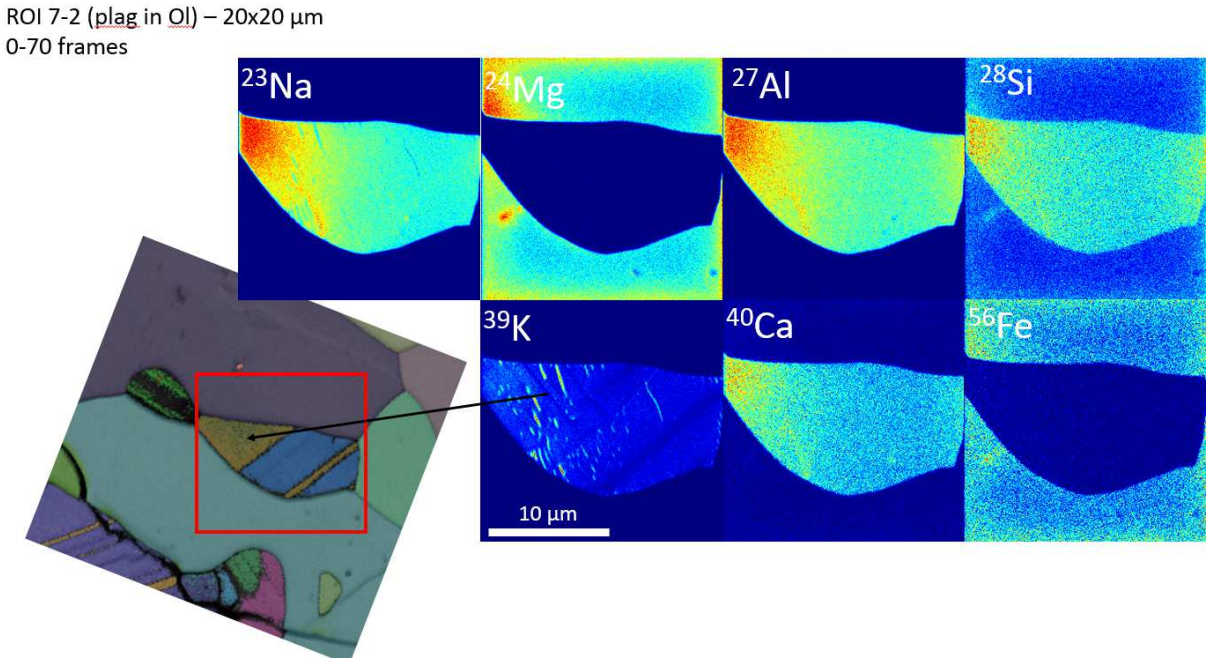


**Fig. S33**: *EBSD map (all euler) and 20 x 20 µm FIB-ToF-SIMS maps (0-70 frames) of selected elements from ROI 7-2 from particle #0010 from a small plagioclase crystal within olivine.*

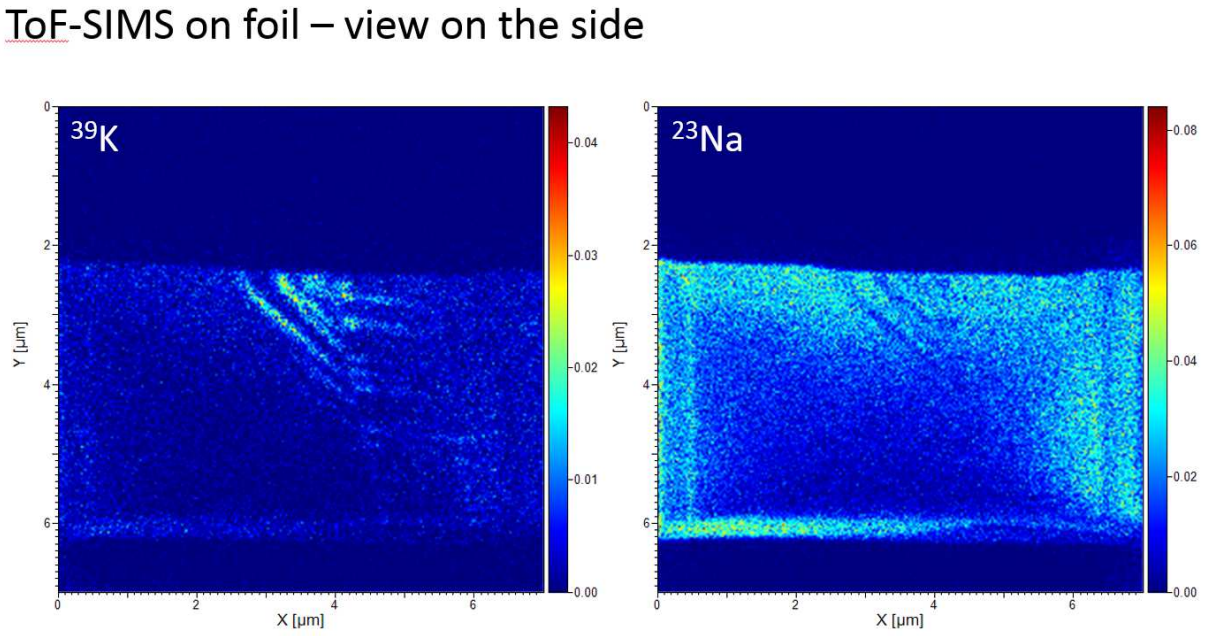


**Fig. S34**: *FIB-ToF-SIMS $^{39}K$ and $^{23}Na$ maps of plagioclase from particle #0010 in depth (cross-section) showing the morphology of the K-feldspar exsolutions in 3D.*

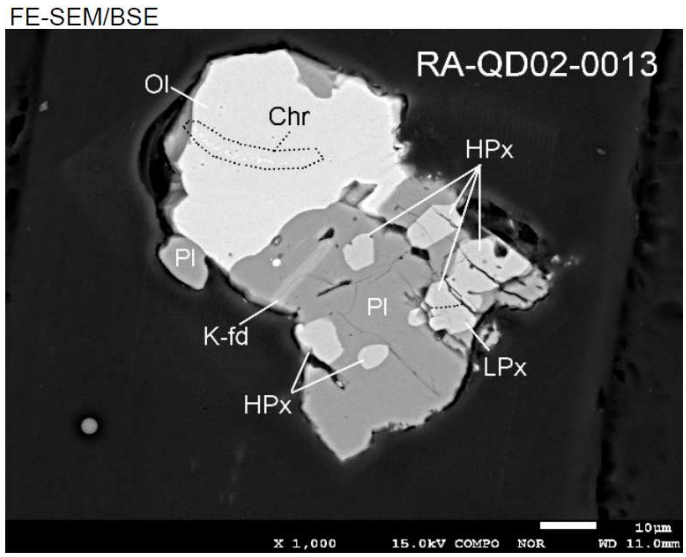


**Fig. S35**: *Crystal phases of particle #0013 measured by SEM and EDX (Courtesy of JAXA; 1) and shown here for comparison. This image shows a single large exsolution of K-feldspar which is different in shape and size from the feather-like K-feldspar exsolutions of particle #0010 (this study).*

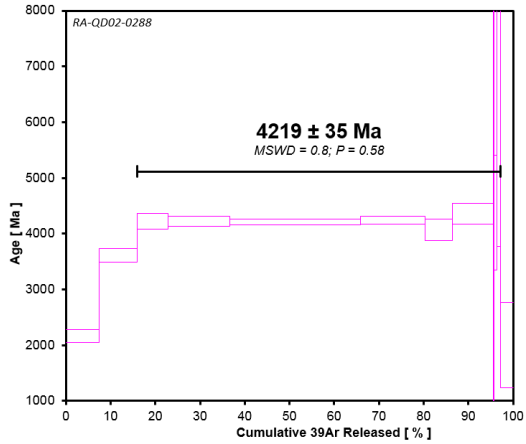


**Fig. S36**: *Age spectrum of particle #0288 showing an 81% plateau age at ~4.2 Ga.*

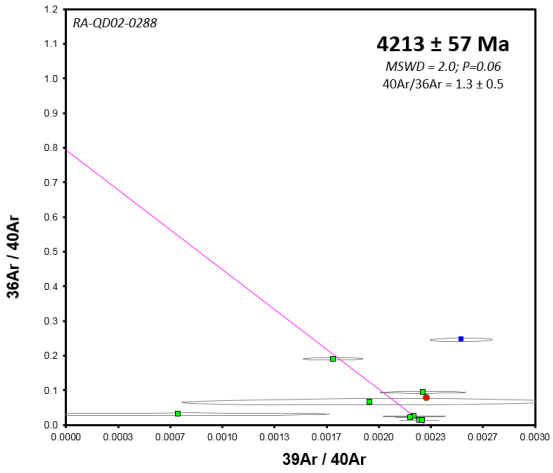


**Fig. S37**: *Inverse isochron plot for particle #0288. The inverse isochron includes 81% of the total $^{39}Ar$ gas released (green-filled square) but is essentially a 2.5-point isochron.*

The K/Ca plot shows slight variation above background with measurable steps values ranging from ca. 0.3 to 0.0017 (Fig. S38; Dataset S2).

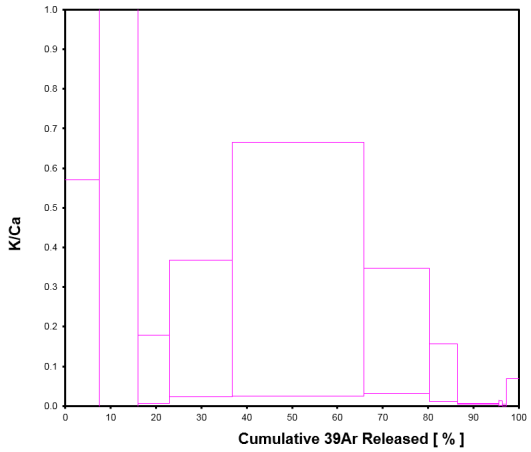

**Fig. S38**: *K/Ca plot for particle #0288.*

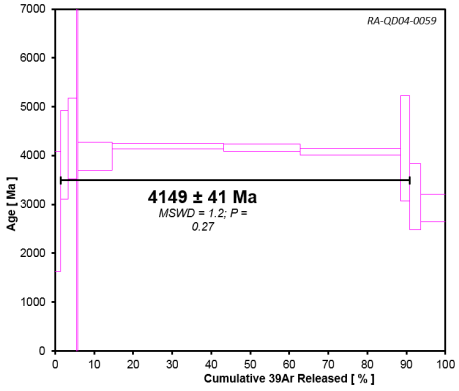


**Fig. S39**: *Age spectrum of particle #0059 showing an 89% plateau age at ~4.2 Ga.*

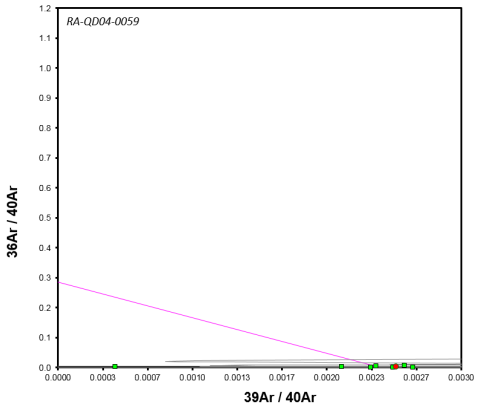


**Fig. S40**: *Inverse isochron plot for particle #0059 where no age could be calculated due to the lack of spread along the line.*

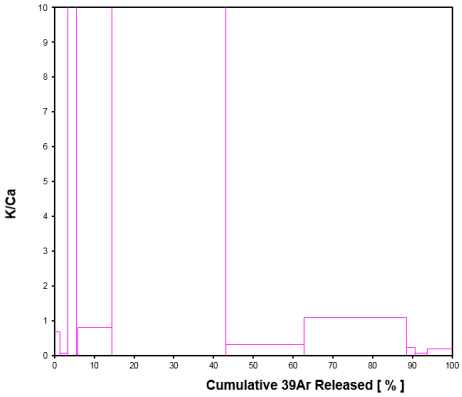


**Fig. S41**: *K/Ca plot for particle #0059.*

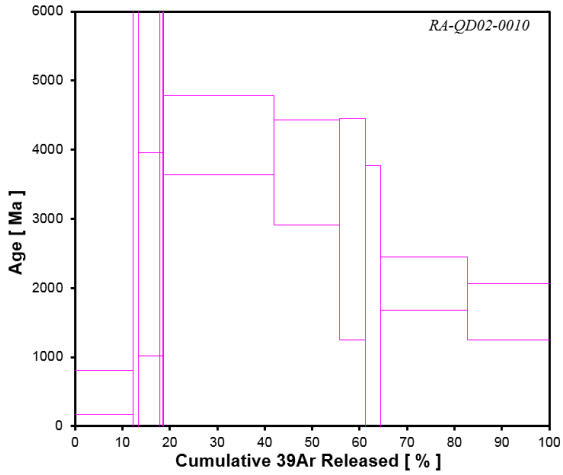


**Fig. S42**: *Age spectrum of particle #0010. No age could be calculated.*

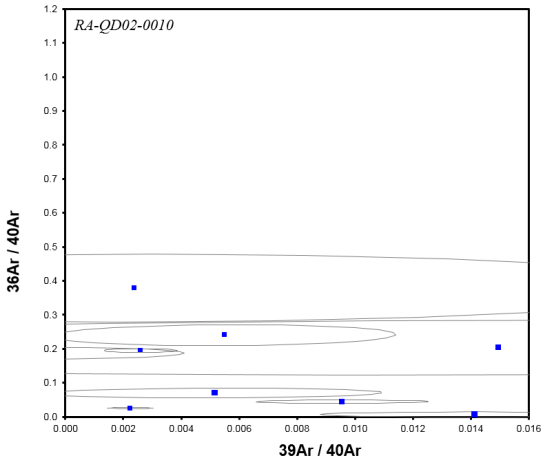


**Fig. S43**: *Inverse isochron plot for particle #0059 where no age could be calculated due to the scatter of the data*

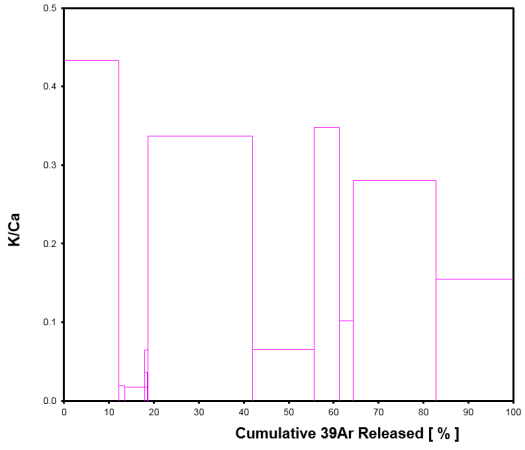


**Fig. S44**: *K/Ca plot for particle #0010.*

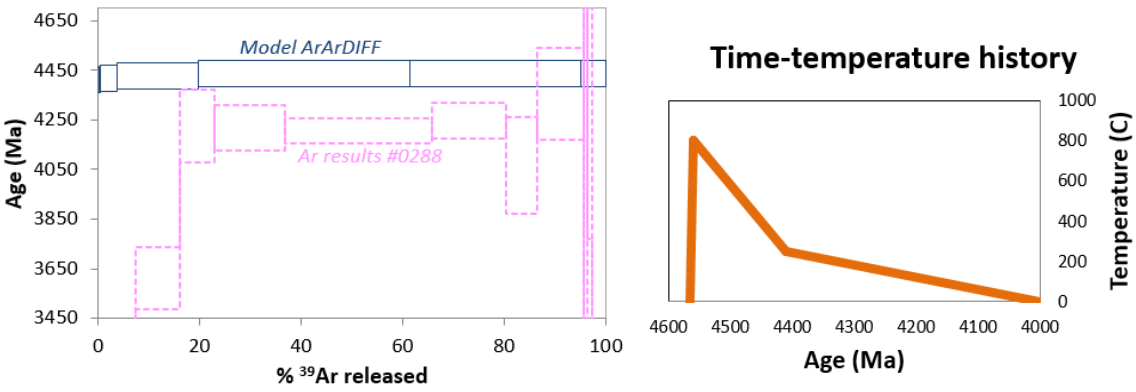


**Fig. S45**: *Modelled age spectra for a 20 µm radius sphere with an albite composition ($D_0$ and $E_a$ values are given in the text) that simulate slow cooling inside a monolithic parent asteroid. The thermal history of the crystal is provided in the text and in the right panel and consists in a brief heating episode to peak metamorphic conditions followed by slow cooling inside the monolithic asteroid (details in the text).*

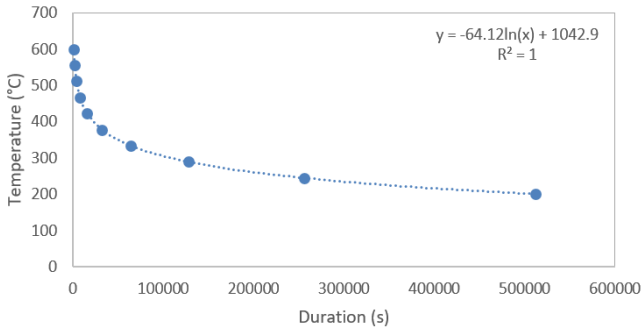


**Fig. S46**: *Cooling curve following a logarithmic decay used in the T-t history calculation of a particle.*

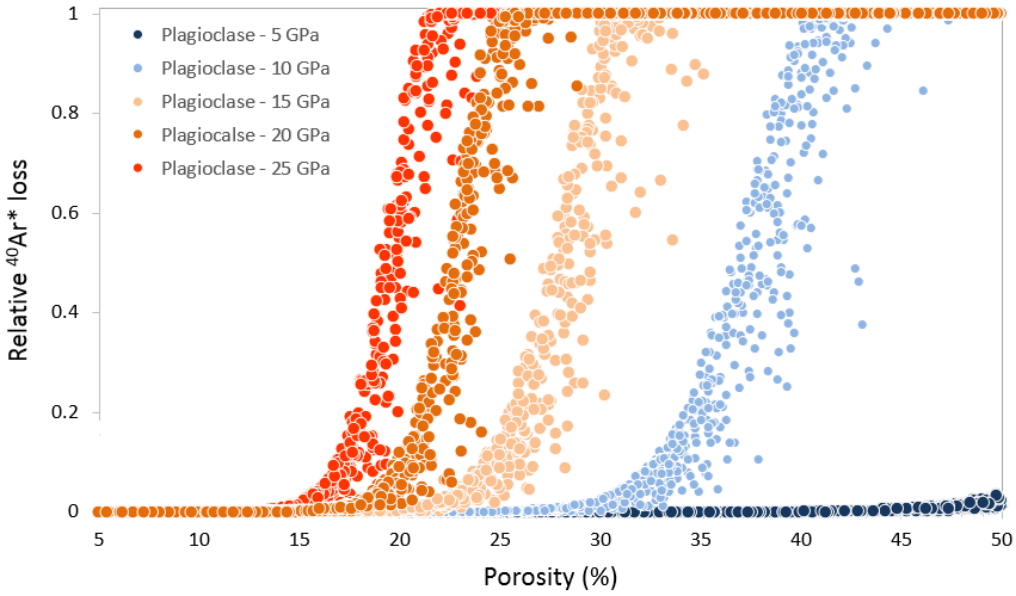


**Fig. S47**: *Monte Carlo simulations of the relative amount of $^{40}$Ar* loss in function of porosity and shock pressure. Only pressure levels higher than 8-10 GPa with porosity of 41-50 % can produce temperatures high enough (~ 920 °C; Fig. 3) to cause full reset of the K/Ar system. Higher level of pressure requires proportionally less amount of porosity.*

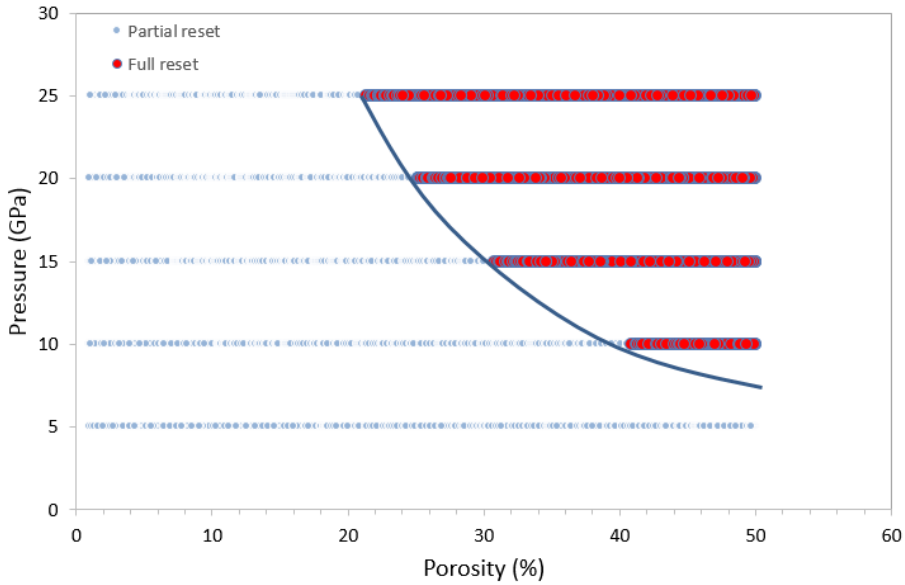


**Fig. S48**: *Monte Carlo simulations of the required amount of pressure vs. porosity to fully reset the K/Ar systematic of plagioclase crystals. Partial and Full $^{40}$Ar* loss are indicated by small blue and large red circles, respectively. Boundary showing the minimum Pressure-porosity value to fully reset plagioclase is indicted by a blue line. Fig. 3 shows that this line corresponds to a temperature of 920 °C.*

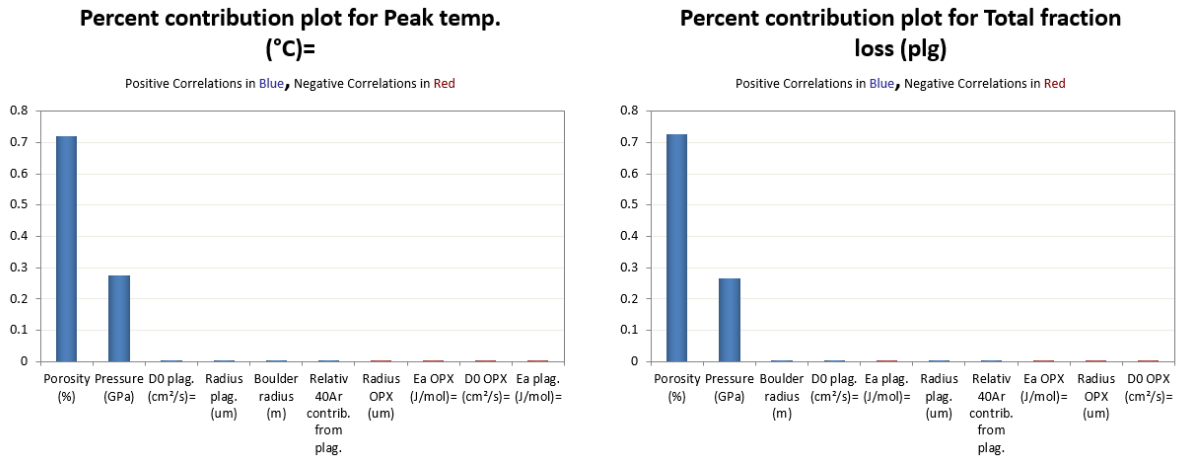


**Fig. S49**: *Tornado charts showing the relative weight of the factors contributing to the variation in maximum post-shock temperature, and thus, the loss of $^{40}Ar^*$ in the plagioclase as calculated from our shock-temperature-porosity model (1). Adding the values of all the boxes sum to one. Positive correlations with diffusion loss are indicated in blue, negative correlations are indicated in red.*

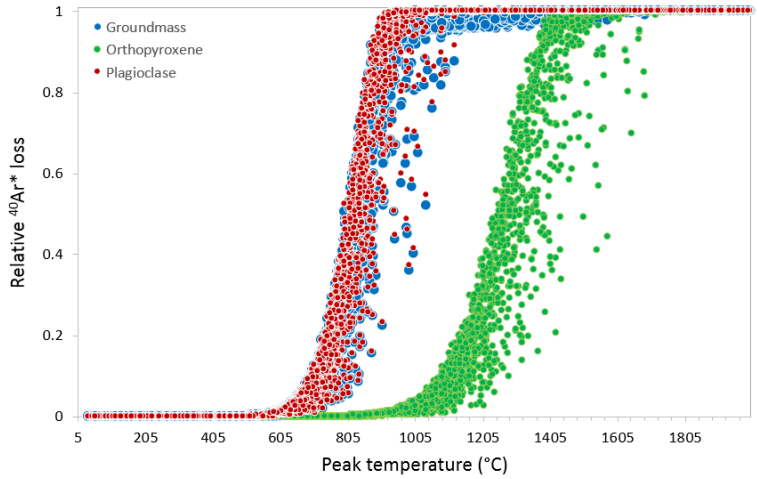


**Fig. S50**: *Monte Carlo simulations of $^{40}Ar^*$ loss vs. temperature (calculated from a pressure-porosity model; Jourdan et al., 2017) for plagioclase (red), orthopyroxene (green) and a resulting plagioclase-orthopyroxene (groundmass) particle with the $^{40}Ar^*$ contribution of plagioclase within the groundmass simulated to range between 95 and 100%.*

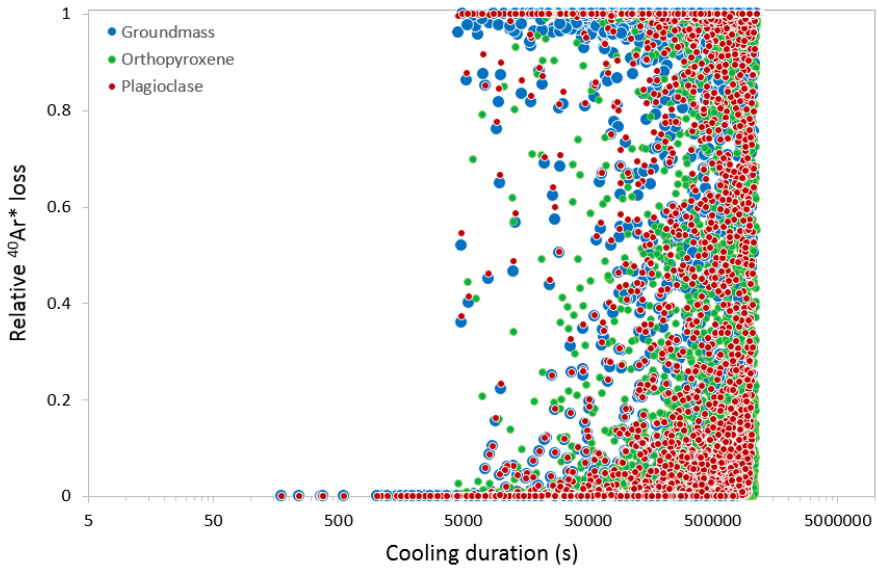


**Fig. S51**: *Monte Carlo simulations of $^{40}$Ar* loss vs. cooling duration for plagioclase (red), orthopyroxene (green) and a resulting plagioclase-orthopyroxene (groundmass) particle (cf. Fig. S4, S9 and S14). Note the lack of correlation between the two, suggesting that the cooling duration plays a minor role in the process associated with $^{40}$Ar* loss.*

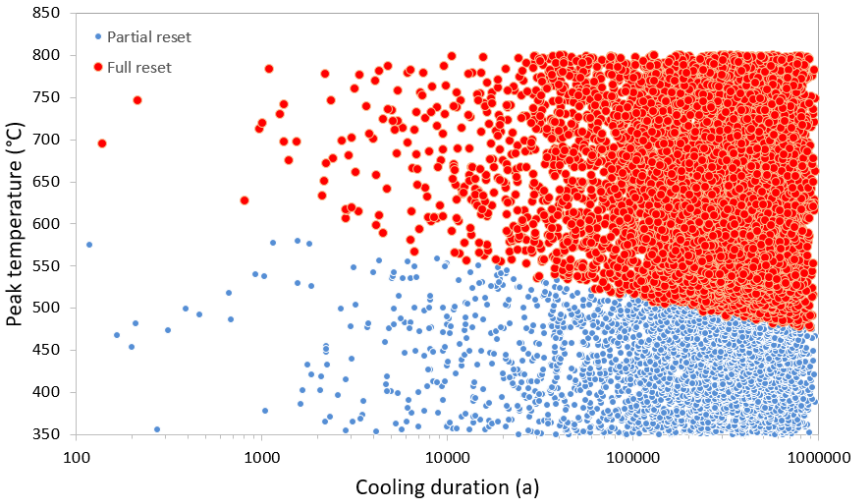


**Fig. S52**: *Monte Carlo simulations of the required peak temperature vs. cooling time required to fully reset the K/Ar systematic of plagioclase crystals. Partial and Full $^{40}$Ar* loss are indicated by small blue and large red circles, respectively. Note x-axis in logarithmic scale*

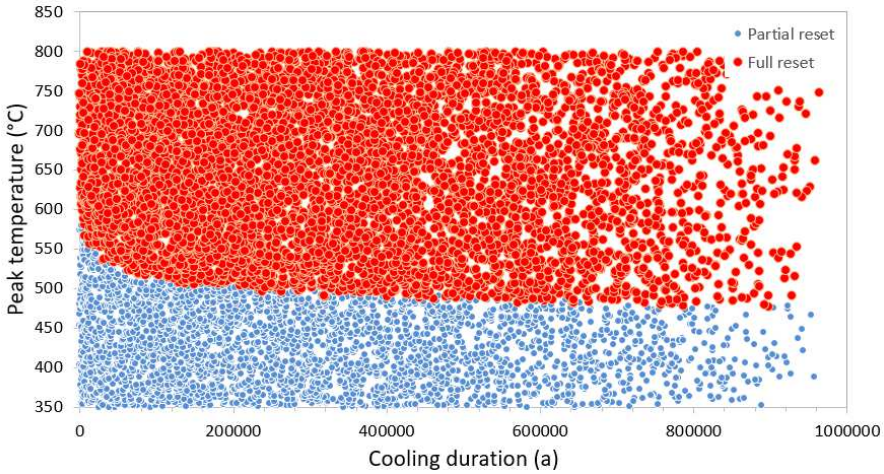


**Fig. S53**: *Monte Carlo simulations of the required peak temperature vs. cooling time required to fully reset the K/Ar systematic of plagioclase crystals, similar to Fig. S52 but presented using a linear scale on x-axis to help visualize the lesser effect of longer cooling durations on $^{40}Ar^*$ loss compared to the peak temperature values.*

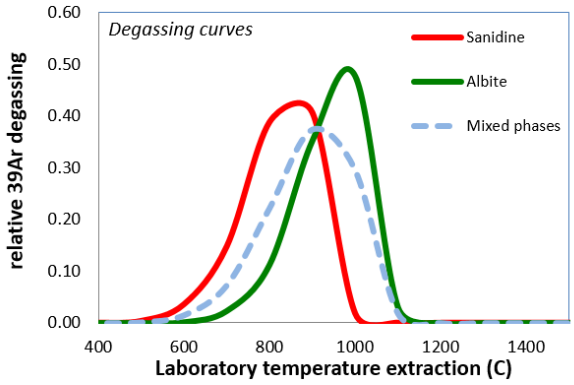


**Fig. S54**: *Theoretical laboratory degassing curves for albite and sanidine based on diffusion and sphere size given above. The dash curve represents the behaviour of a particle including all those phases and relative to the amount of $^{40}Ar^*$ given by each component.*

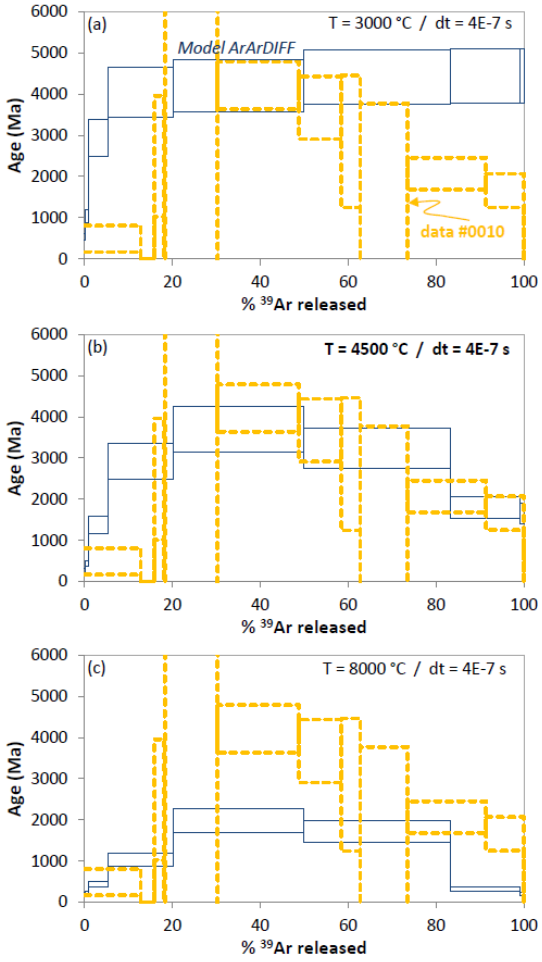


**Fig. S55**: *Modelled age spectra for a mixture of a 25 µm radius sphere with an albite composition comprising 60% of the $K_2O$ and a 3µm radius sphere with a sanidine composition comprising 40% of the total $K_2O$ ($D_0$ and $E_a$ values are given in the text). The composite mixture has been heated by an impact shock at ultra-transient (0.4 µs) square pulse peak temperatures of 3000, 4500, 8000 °C. Cooling from the peak temperature to 0°C is considered instantaneous.*

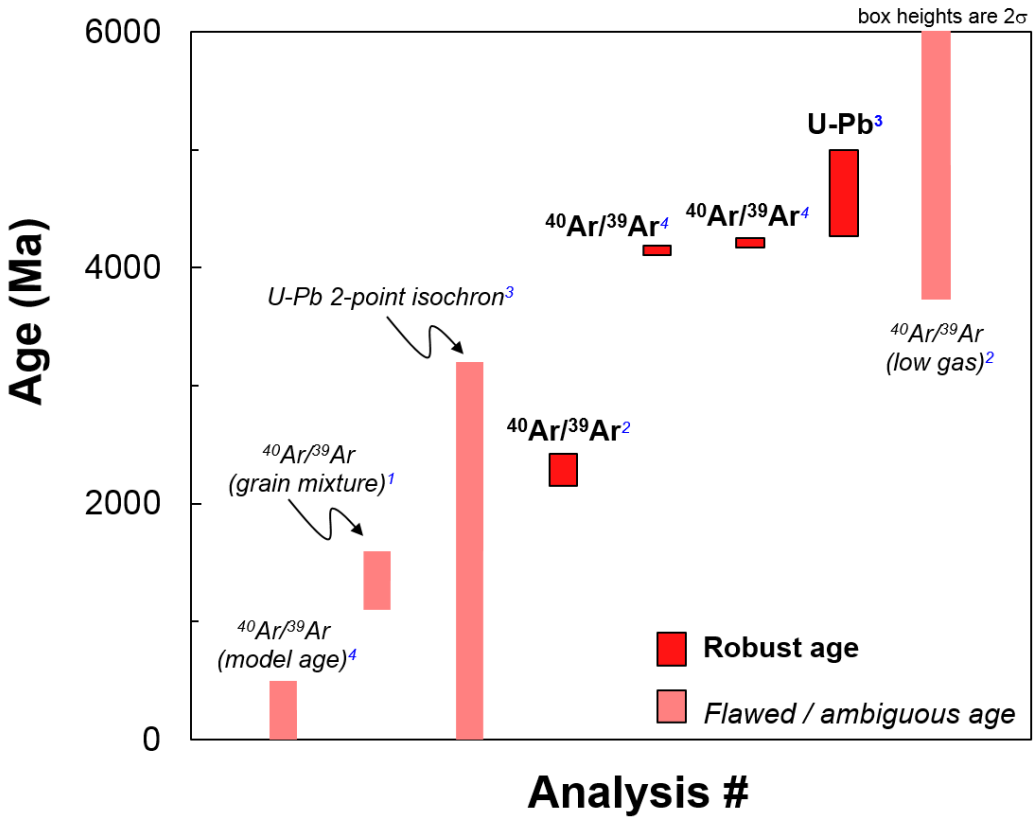


***Fig. S56**: All available isotopic geochronological results obtained on Itokawa particles. The robustness of these ages is inequal and some of them have very little geological meaning as discussed in the text. As a result, only four isotopic ages can safely be used to understand the geochronological history of Itokawa. References: [1](27), [2](1), [3](26), [4](this study).*

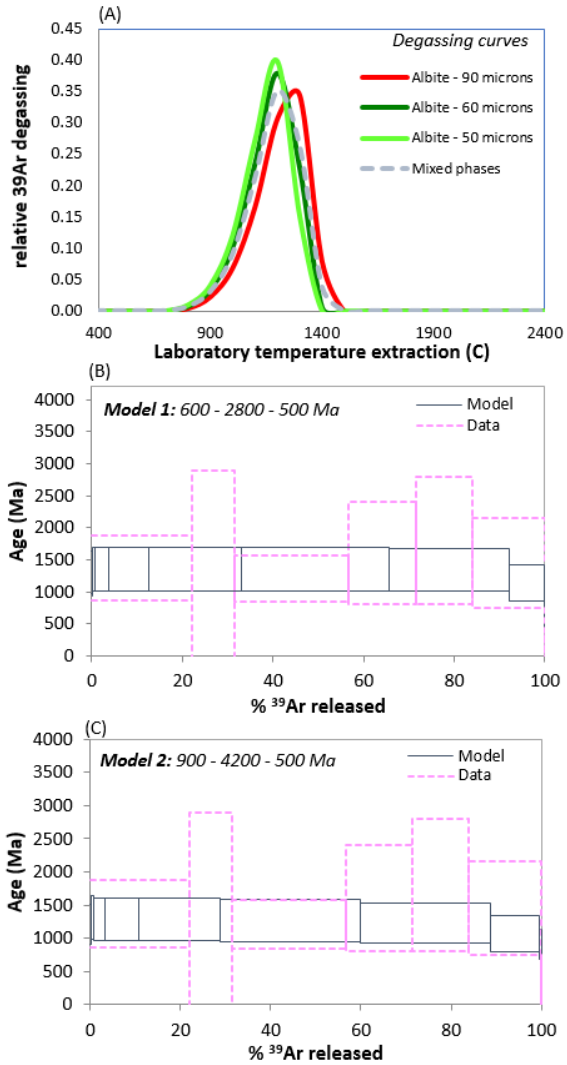


**Fig. S57**: *Modelled age spectra for a mixture of a 90, 60 and 50 µm radius spheres with an albite composition. (A) degassing curves of each particle during laboratory extraction. (B) and (C) ArArDIFF model (blue solid-line boxes) vs. $^{40}Ar/^{39}Ar$ data measured by (27) (Pink dash-line boxes). (B) model 1: mixture comprising three particles with 44, 33 and 22% of the $^{40}Ar^*$ contribution and arbitrary ages of 600, 2800, 500 Ma, respectively. (C) model 2: mixture comprising three particles with 85, 15 and 5% of the $^{40}Ar^*$ contribution and arbitrary ages of 9200, 4200, 500 Ma, respectively.*

| Element | Phase | | | | | | | | | |
|---|---|---|---|---|---|---|---|---|---|---|
| | Olivine | | Plagioclase | | Troilite | | Taenite | | Kamacite | |
| | Spectrum 16 | | Spectrum 17 | | Spectrum 18 | | Spectrum 19 | | Spectrum 20 | |
| | Wt% | At% | Wt% | At% | Wt% | At% | Wt% | At% | Wt% | At% |
| O | 40.6 | 57.3 | 48.4 | 61.5 | 42.7 | 67.0 | 21.9 | 50.0 | 22.6 | 50.5 |
| Si | 18.1 | 14.6 | 30.8 | 22.3 | | | | | | |
| Fe | 19.2 | 7.8 | 0.1 | 0.0 | 35.2 | 15.8 | 38.2 | 25.0 | 69.3 | 44.4 |
| Mg | 22.0 | 20.4 | | | | | | | | |
| Al | | | 11.3 | 8.5 | 0.1 | 0.1 | 0.1 | 0.1 | | |
| Ca | | | 1.0 | 0.5 | | | | | | |
| K | | | 0.3 | 0.2 | | | | | | |
| Na | | | 8.0 | 7.1 | | | | | | |
| S | | | | | 21.7 | 17.0 | | | 0.4 | 0.5 |
| Ni | | | | | | | 37.6 | 23.4 | 3.0 | 1.8 |
| Co | | | | | | | 2.2 | 1.4 | 4.8 | 2.9 |
| Cu | | | | | 0.3 | 0.1 | | | | |

***Table S1**: EDX measurements of the various crystal phases shown in Fig. S5 and indicating a K composition of 0.3 wt% for plagioclase.*

**RA-QD02-0288** 80 nm map detected elements

| Element | Phase | | | | | | | |
|---|---|---|---|---|---|---|---|---|
| | Ca-rich Px | | Ca-poor Px | | Olivine | | Plagioclase | |
| | Spectrum 2 | | Spectrum 4 | | Spectrum 5 | | Spectrum 6 | |
| | Wt% | At% | Wt% | At% | Wt% | At% | Wt% | At% |
| O | 43.2 | 59.6 | 44.1 | 59.6 | 40.5 | 57.2 | 48.2 | 61.5 |
| Si | 26.1 | 20.5 | 26.3 | 20.3 | 18.2 | 14.6 | 30.3 | 22.0 |
| Fe | 4.5 | 1.8 | 11.5 | 4.4 | 19.3 | 7.8 | 0.3 | 0.1 |
| Mg | 10.4 | 9.4 | 16.9 | 15.0 | 22.0 | 20.5 | | |
| Al | | | | 0.1 | | | 11.6 | 8.7 |
| Ca | 14.6 | 8.0 | 0.8 | 0.4 | | | 1.5 | 0.7 |
| K | | | | | | | 0.8 | 0.4 |
| Na | 0.4 | 0.4 | | | | | 7.4 | 6.6 |
| Mn | | | 0.3 | 0.1 | | | | |
| Cr | 0.6 | 0.2 | | | | | | |
| Ti | 0.3 | 0.1 | 0.1 | 0.1 | | | | |

***Table S2**: EDX measurements of the various crystal phases shown in Fig. Sx and showing a K composition of 0.8 wt% for plagioclase.*

**RA-QD02-0010** 80 nm map detected elements

| Element | Phase | | | | | | | | | | | | | |
|---|---|---|---|---|---|---|---|---|---|---|---|---|---|---|
| | Olivine | | Plagioclase | | High-Ca Px | | Low-Ca Px | | Taenite | | Taenite (mixed) | | Troilite | |
| | Spectrum 1 | | Spectrum 2 | | Spectrum 3 | | Spectrum 4 | | Spectrum 6 | | Spectrum 7 | | Spectrum 5 | |
| | Wt% | At% | Wt% | At% | Wt% | At% | Wt% | At% | Wt% | At% | Wt% | At% | Wt% | At% |
| O | 40.7 | 57.3 | 48.2 | 61.5 | 43.9 | 60.1 | 44.2 | 59.7 | 28.8 | 53.5 | 33.5 | 55.3 | 42.5 | 66.9 |
| Si | 18.1 | 14.5 | 30.3 | 22.0 | 25.7 | 20.1 | 25.2 | 19.4 | 6.7 | 7.1 | 11.2 | 10.5 | | |
| Fe | 19.0 | 7.7 | 0.1 | 0.1 | 4.2 | 1.7 | 12.1 | 4.7 | 28.6 | 15.2 | 24.7 | 11.7 | 35.6 | 16.1 |
| Mg | 22.2 | 20.6 | | | 10.2 | 9.2 | 17.9 | 15.9 | 8.4 | 10.2 | 13.8 | 14.9 | | |
| Al | | | 11.6 | 8.8 | 0.4 | 0.3 | | | | | | | | |
| Ca | | | 1.5 | 0.8 | 14.4 | 7.9 | 0.3 | 0.2 | | | | | | |
| K | | | 0.8 | 0.4 | | | | | | | | | | |
| Na | | | 7.4 | 6.5 | 0.4 | 0.4 | | | | | | | | |
| Mn | | | | | | | 0.3 | 0.1 | | | | | | |
| S | | | | | | | | | | | | | 21.5 | 16.9 |
| Ni | | | | | | | | | 27.6 | 14.0 | 16.9 | 7.6 | | |
| Cr | | | | | 0.5 | 0.2 | | | | | | | | |
| Ti | | | | | 0.3 | 0.1 | | | | | | | | |
| Cu | | | 0.0 | 0.0 | | | | | | | | | 0.3 | 0.1 |

***Table S3****: EDX measurements of the various crystal phases from domains shown in Fig. S14, and showing a K composition of 0.8 wt% for plagioclase similar to the value of ~0.9 wt% measured by the more accurate EMPA measurements.*

| Process Inputs | | |
|---|---|---|
| Radius plag. (um) | Mean | StDev |
| Distribution: **Normal** | 20 | 1 |
| D0 plag. ($cm^2/s$)= | Mean | StDev |
| Distribution: **Normal** | 5000 | 100 |
| Ea plag. (J/mol)= | Mean | StDev |
| Distribution: **Normal** | 290000 | 1000 |
| Relativ 40Ar contrib. from pl | Lower | Upper |
| Distribution: **Uniform** | 0.95 | 1 |
| Radius OPX (um) | Mean | StDev |
| Distribution: **Normal** | 30 | 2 |
| D0 OPX ($cm^2/s$)= | Mean | StDev |
| Distribution: **Normal** | 600 | 5 |
| Ea OPX (J/mol)= | Mean | StDev |
| Distribution: **Normal** | 371000 | 2000 |
| Porosity (%) | Lower | Upper |
| Distribution: **Uniform** | 1 | 50 |
| Boulder radius (m) | Lower | Upper |
| Distribution: **Uniform** | 0.1 | 25 |

**Table S4***: Parameters and distribution used in the Monte Carlo simulations of the relative amount of $^{40}Ar^*$ loss in function of porosity and shock pressure.*

**Diffusion parameters**

| | $D_0$ ($cm^2/s$) | $E_a$ (J/mol) | Radius (µm) | *Mixed phases* Modal composition | %$K_2O$ for each mineral | $K_2O$ contribution (mixed phase) |
|---|---|---|---|---|---|---|
| Sanidine | 6.70E-01 | 220000 | 3 | 5% | 10% | 40% |
| Albite | 5.00E+03 | 290000 | 25 | 95% | 1% | 60% |

**Thermal history**

| | | | Peak Temperature | |
|---|---|---|---|---|
| Crystallization age | 4560 | Ma | Model a: 3000 | °C |
| Impact age | 200 | Ma | Model b: 4500 | °C |
| Duration | 4.0E-07 | s | Model c: 8000 | °C |

**Table S5**: *Parameters used in the ArArDIFF diffusion simulation for a mixture of sanidine and albite heated during a transient by an impact shock and shown in Fig. S55.*